AGU PUBLICATIONS

JGR

Journal of Geophysical Research: Oceans

RESEARCH ARTICLE

10.1002/2015JC010806

On the role of infiltration and exfiltration in swash zone boundary layer dynamics

José Carlos Pintado-Patiño[1], Alec Torres-Freyermuth[1], Jack A. Puleo[2], and Dubravka Pokrajac[3]

[1]Laboratorio de Ingeniería y Procesos Costeros, Instituto de Ingeniería, Universidad Nacional Autónoma de México, Sisal, Yucatán, México, [2]Ocean Engineering Laboratory, Center for Applied Coastal Research, Department of Civil and Environmental Engineering, University of Delaware, Newark, Delaware, USA, [3]School of Engineering, King's College, University of Aberdeen, Aberdeen, UK

Key Points:
- Model reproduces swash zone hydrodynamics on permeable bed
- Vorticity is used to investigate the boundary layer evolution in the swash
- Existing boundary layer theory is not applicable when infiltration is dominant

Correspondence to:
A. Torres-Freyermuth,
ATorresF@iingen.unam.mx

Citation:
Pintado-Patiño, J. C., A. Torres-Freyermuth, J. A. Puleo, and D. Pokrajac (2015), On the role of infiltration and exfiltration in swash zone boundary layer dynamics, *J. Geophys. Res. Oceans*, *120*, 6329–6350, doi:10.1002/2015JC010806.

Received 27 FEB 2015
Accepted 16 AUG 2015
Accepted article online 19 AUG 2015
Published online 19 SEP 2015

Abstract Boundary layer dynamics are investigated using a 2-D numerical model that solves the Volume-Averaged Reynolds-Averaged Navier-Stokes equations, with a VOF-tracking scheme and a k - ϵ turbulence closure. The model is validated with highly resolved data of dam break driven swash flows over gravel impermeable and permeable beds. The spatial gradients of the velocity, bed shear stress, and turbulence intensity terms are investigated with reference to bottom boundary layer (BL) dynamics. Numerical results show that the mean vorticity responds to flow divergence/convergence at the surface that result from accelerating/decelerating portions of the flow, bed shear stress, and sinking/injection of turbulence due to infiltration/exfiltration. Hence, the zero up-crossing of the vorticity is employed as a proxy of the BL thickness inside the shallow swash zone flows. During the uprush phase, the BL develops almost instantaneously with bore arrival and fluctuates below the surface due to flow instabilities and related horizontal straining. In contrast, during the backwash phase, the BL grows quasi-linearly with less influence of surface-induced forces. However, the infiltration produces a reduction of the maximum excursion and duration of the swash event. These effects have important implications for the BL development. The numerical results suggest that the BL growth rate deviates rapidly from a quasi-linear trend if the infiltration is dominant during the initial backwash phase and the flat plate boundary layer theory may no longer be applicable under these conditions.

1. Introduction

The swash zone is commonly identified as the alternating wet/dry interface at the beach face resulting from the intermittent sequence of inundating/receding wave-driven flows. Thus, it is an active region of morphological change where sediment exchange between the subaerial and subaqueous beach profile occurs. In addition, the alongshore component of the sediment motion can be significant under some conditions [*Wang et al.*, 2002; *Austin et al.*, 2011; *Puleo et al.*, 2014a]. The swash zone is the most accessible, frequently used region of the nearshore for recreational purposes. Yet our knowledge of the sediment transport processes that occur in this dynamic region is hampered by the difficulty in fully measuring the transient, depth and alongshore variant, turbulent flows [e.g., *Butt and Russell*, 1999; *Masselink and Puleo*, 2006, among many others]. In addition, the local mass and momentum transfer at the sediment-water interface of the beach varies on swash-by-swash and tidal cycle time scales [*Li et al.*, 1997; *Turner and Nielsen*, 1997]. These variations lead to infiltration/exfiltration effects and groundwater fluctuations that may be important for sediment mobility [*Turner and Masselink*, 1998; *Butt et al.*, 2001; *Nielsen et al.*, 2001]. Thus, determining the effects of bed sediment characteristics (i.e., permeability and porosity) on boundary layer evolution is an important step toward improved understanding and predictive capability of swash-zone sediment transport.

Previous studies have investigated the mean and turbulent flow field during the different phases of an individual swash cycle under natural [*Puleo et al.*, 2000; *Butt et al.*, 2004; *Aagaard and Hughes*, 2006; *Raubenheimer et al.*, 2004; *Blenkinsopp et al.*, 2011; *Puleo et al.*, 2014b; *Lanckriet et al.*, 2014] and laboratory [*Cowen et al.*, 2003; *Barnes et al.*, 2009; *O'Donoghue et al.*, 2010; *Sou et al.*, 2010; *Sou and Yeh*, 2011; *Kikkert et al.*, 2012, 2013] conditions. Moreover, recent numerical studies [e.g., *Brocchini and Baldock*, 2008; *Bakhtyar et al.*, 2009; *Zhu and Dodd*, 2013; *Torres-Freyermuth et al.*, 2013] have provided additional information on the

dynamics in this region, as they allow improved understanding of temporal and spatial variability of flow properties under different boundary/forcing conditions. From these studies, a general description of the swash cycle in relation to sediment transport is synthetized as follows. Injection of bore related turbulence contributes to the cross-shore advection of particles into the swash zone that, together with the local mobilization, are effective in transporting sediment during swash cycle initiation [*Butt and Russell*, 1999; *Puleo et al*., 2000; *Petti and Longo*, 2001; *Jackson et al*., 2004; *Masselink et al*., 2005; *Aagaard and Hughes*, 2006]. During the remainder of the decelerating uprush motion, the turbulence decays similar to grid turbulence [*Cowen et al*., 2003; *Sou and Yeh*, 2011; *Lanckriet and Puleo*, 2013] and more homogeneously [*Zhang and Liu*, 2008] as the flow reaches the maximum inundation limit toward land (e.g., run up distance). Hence, sediment particles are more likely to settle during the flow reversal phase. Shortly afterward, the flow evolves from subcritical to supercritical as the favorable pressure gradient becomes increasingly stronger during the backwash phase [*Baldock and Hughes*, 2006]. Sediment transport is then dominated by bed-generated turbulence [*Longo et al*., 2002; *Cowen et al*., 2003; *Zhang and Liu*, 2008; *Lanckriet and Puleo*, 2013] that may also mobilize sediment as sheet flow [*Hughes et al*., 2007; *Lanckriet et al*., 2014]. The relative dominance of the different flow phases (i.e., uprush versus backwash asymmetry) during a swash cycle largely depends on the beach face slope and incident wave conditions [*Masselink and Puleo*, 2006] and is known to have a large influence controlling the overall morphological response of the beach [*Osborne and Rooker*, 1999; *Blenkinsopp et al*., 2011; *Puleo et al*., 2014a; *Masselink et al*., 2009].

One of the largest limitations in the study of swash-zone sediment transport relates to the challenge of measuring the bottom boundary layer (BL) structure for the highly unsteady and depth-variant swash flow conditions. Under such constraints, the numerical approach has been useful to examine/test conceptual boundary layer models specifically applied to the swash zone. Previous studies have derived the time dependent swash BL thickness based on the nonlinear shallow water (NLSW) equations. For instance, *Barnes and Baldock* [2010] solved the Prandtl and von Karman's approach of the momentum integral turbulent flat-plate bottom boundary layer (FPBL) in a Lagrangian reference frame, allowing a quasi-steady treatment of the flow. *Briganti et al*. [2011] solved the momentum integral method for the turbulent BL of *Fredsøe and Deigaard* [1992] in an Eulerian reference frame. Both studies suggest that the swash BL varies in the following sequence: (i) immediate initial growth that at times becomes depth-limited around the tip of the fluid during the uprush; (ii) BL thickness decays as do the velocities and turbulence during flow reversal; and (iii) progressive BL growth until becoming depth-limited at later stages of backwash while the BL evolves from laminar to turbulent. A limitation in the aforementioned studies is their reliance on the assumption that the log law prevails inside the BL. This assumption has been commonly employed in field studies [e.g., *Raubenheimer et al*., 2004; *Masselink et al*., 2005], based on single point or coarse velocity measurements, leading to consistent estimates of bed shear stresses and friction coefficients. However, laboratory based studies of swash flows over fixed beds have concluded that the log law does not predict adequately the leading and trailing edges of the bore front [*Barnes et al*., 2009], and the near flow reversal phases [*Cox et al*., 2001; *Archetti and Brocchini*, 2002; *O'Donoghue et al*., 2010; *Kikkert et al*., 2012]. Thus, the suitability of this assumption under natural settings may be limited to certain flow conditions [*Puleo et al*., 2012, 2014a] as confirmed by field measurements of near bed velocity profiles at a high-resolution (100 Hz at 1 mm vertical spacing).

Earlier works [*Nielsen*, 1992; *Conley and Inman*, 1994; *Turner and Nielsen*, 1997; *Turner and Masselink*, 1998; *Hughes and Turner*, 1999; *Butt et al*., 2001] related the behavior of the streamlines of the flow with the infiltration/exfiltration of water into/from ventilated natural beds. From these and other studies [e.g., *Packwood and Peregrine*, 1979; *Li et al*., 2000; *Nielsen et al*., 2001; *Karambas*, 2003] it is established that one of the main effects of the infiltrating/exfiltrating flows relates to the mass and momentum transfer that result from these motions, affecting the magnitudes of the bed shear stress and the BL thickness. Additionally, these fluxes are responsible for the suction/injection of turbulence and, consequently, for the thinning/spreading of the BL [*Lohmann et al*., 2006; *Sparrow et al*., 2012; *Kikkert et al*., 2013; *Corvaro et al*., 2014]. The continuity effect [after *Baldock and Nielsen*, 2010; *Kikkert et al*., 2013] denotes the modification of the momentum balance due to losses of water volume in the surface flow that may also indirectly affect the bed shear stress. *Steenhauer et al*. [2011] and *Kikkert et al*. [2013] reported water losses at the time of maximum run up of up to 45% to 50% for a permeable gravel bed during one dam break driven swash event. Another important effect related to the infiltration/exfiltration is the alteration of drag forces

and potential for sediment mobility, as the effective weight of the upper elements of the bed are also modified. This effect has been addressed as the stabilization/destabilization of the bed [for reviews, see *Baldock et al*. [2001] and *Horn* [2006]). In summary, the mechanisms that affect the BL have been identified but still, it is difficult to assess which of the aforementioned effects are dominant under varied conditions. Furthermore, most of studies under controlled settings have been performed over impermeable or fixed beds, implying that the influence of the bed characteristics requires further study.

In this paper, experimental data sets, consisting of dam-break-driven flows over impermeable [*Kikkert et al*., 2012] and permeable [*Kikkert et al*., 2013] fixed beds, are used to validate a numerical model for its use inside the swash zone. We further investigate the effects of bed characteristics on swash zone boundary layer dynamics by quantifying the differences in the mean and turbulence flow fields. The paper is organized as follows. Section 2 provides a brief description of the dam break experiment data used for the numerical validation. The description of the numerical model, setup of simulated cases, and model calibration are presented in section 3. The results from the model-data comparisons are presented in section 4. The model validation is followed by a comparative analysis between the impermeable and permeable cases with special attention in the near bed flow properties. The results from the numerical investigation are provided within section 5. Then, the discussion (section 6) focuses on different approaches for the determination of swash zone BL related quantities. Finally, the main outcomes of the present study are summarized in section 7.

2. Experimental Layout

The data sets used for the model validation correspond to the laboratory experiments conducted by *Kikkert et al*. [2012, 2013] and hence only a general overview is here provided. The experimental setup consists of a wave flume facility with dimensions of 20 m long, 0.9 m high, and 0.45 m wide. A mass of water 0.6 m deep (h_d), 1 m long, and 0.45 m wide is confined at one end of the flume by a movable gate. The gate is designed to be raised at high speed, releasing the confined mass of water onto a flat horizontal section (4.2 m long). The initial still water level above the flat horizontal section is 0.062 m deep (h_o). A 1:10 sloping beach extends from 4.2 to 10.8 m from the gate. Thus, an individual swash event is generated by raising the dividing gate between the reservoir and the flat section. A plunging breaker is then produced that evolves into a $\sim$0.25 m high bore. The bore propagates across the flat section until it reaches the beach slope and initiates the swash motion.

The beach is composed of gravel or sand with median (d_{50}) grain sizes of 8.4 mm and 1.5 mm, respectively. For the impermeable tests the sediment particles were glued to a plywood sheet. For the permeable tests the beach was composed of sediment throughout its entire depth and the top 30 mm of sediment were cemented with a dilute water-cement mixture [*Steenhauer et al*., 2011; *Kikkert et al*., 2013] so they remain fixed. The present study focuses on the coarse grain condition only ($d_{50} = 8.4$ mm) since the flow inside the porous media is expected to be stronger, the infiltration/exfiltration effects more evident, and the effects of the air entrapment below the wetting front are very small [*Steenhauer et al*., 2012a,b].

Cross-correlation particle image velocimetry (PIV) and laser induced fluorescence (LIF) techniques were used by *Kikkert et al*. [2012, 2013] in order to measure the vertical profile of the bed-parallel (u_x) and bed-orthogonal (u_x) velocity and instantaneous water depths at 6 cross-shore locations. Ensemble-averaged quantities and turbulence measurements were obtained after repeating identical conditions over 50 tests for PIV/LIF measurements and 10 times for the shoreline motion LIF measurements. For a more detailed description on the experimental techniques and the quality control of the data refer to the original work by *Kikkert et al*. [2012, 2013].

3. Numerical Model

3.1. Mathematical Formulation

The depth- and phase-resolving numerical model COBRAS [*Lin and Liu*, 1998a,b] has been validated for a wide variety of coastal applications, including the study of wave-structure interaction with porous elements [e.g., *Hsu et al*., 2002; *Lara et al*., 2006a,b; *Losada et al*., 2008], and swash-zone hydrodynamics [i.e., *Zhang and Liu*, 2008; *Torres-Freyermuth et al*., 2013]. The model solves the 2-D Volume-Averaged Reynolds-Averaged Navier-Stokes (VARANS) equations given by *Hsu et al*. [2002],

$$\frac{\partial\langle\overline{u_i}\rangle}{\partial x_i}=0, \tag{1}$$

$$\frac{\partial\langle\overline{u_i}\rangle}{\partial t}+\frac{\langle\overline{u_j}\rangle}{\phi(1+C_A)}\frac{\partial\langle\overline{u_i}\rangle}{\partial x_j}=\frac{1}{1+C_A}\left(-\frac{\phi}{\rho}\frac{\partial\langle\overline{p}\rangle^f}{\partial x_i}-\frac{\partial\langle\overline{u_i'u_j'}\rangle}{\partial x_j}+\frac{1}{\rho}\frac{\partial\langle\overline{\tau_{ij}}\rangle}{\partial x_j}+\phi g_i\right) -\frac{1}{1+C_A}\left(\frac{\alpha(1-\phi)^2}{\phi^2 d_{50}^2}\langle\overline{u_i}\rangle+\frac{\beta(1-\phi)}{\phi^2 d_{50}^2}\langle\overline{u_i}\rangle\langle|\overline{u_i}|\rangle\right), \tag{2}$$

where the Reynolds decomposition denotes the separation of mean (—) and fluctuating (′) components, t is the time, x_i is the bed-parallel ($i=1=x$) and bed-orthogonal ($i=2=z$) coordinate, g_i is the gravitational component, u_i is the fluid velocity in direction x_i, ρ is the fluid density, p is pressure, and τ_{ij} is the shear stress of the mean flow. The Reynolds stresses $\rho(\overline{u_i'u_j'})$ are approximated by means of a k-ϵ closure model [*Nakayama and Kuwahara*, 1999; *Hsu et al*., 2002]. The turbulent kinetic energy (TKE) is estimated as $k=\frac{\overline{u_i'u_i'}}{2}$ and the TKE dissipation as $\epsilon=\nu\left[\left(\frac{\partial u_i'}{\partial x_j}\right)^2\right]$, where $\nu=1\times10^{-6}$ m^2 s^{-1} is the kinematic viscosity of the water. The Reynolds stress tensor and the strain rate of the mean flow are related with a nonlinear anisotropic eddy viscosity model [*Shih et al*., 1996; *Lin and Liu*, 1998b]. For the porous media, $C_A=\gamma_p\frac{1-\phi}{\phi}$ is the added mass coefficient after *van Gent* [1994], $\gamma_p=0.34$ is a nondimensional parameter [also referred to as virtual added mass coefficient in *Corvaro et al*. [2010], and the magnitude of the mean component of the velocity is expressed as $|\overline{u_i}|=\sqrt{\overline{u_x}^2+\overline{u_z}^2}$. *Corvaro et al*. [2010] have pointed out the role that a variable C_A can have in the near bed hydrodynamics. However, for simplicity a constant C_A value is adopted here. The effective porosity is defined as $\phi=\frac{V_f}{V}$, where V denotes the total averaging volume, V_f is the portion of V that is occupied by the fluid. The $\langle\rangle$ denote the Darcy's volume averaging operator and $\langle\rangle^f$ the intrinsic averaging operator, both related by $\langle a\rangle=\phi\langle a\rangle^f$ for a quantity a as,

$$\langle a\rangle=\frac{1}{V}\int_{V_f}a\,dV, \tag{3}$$

$$\langle a\rangle^f=\frac{1}{V_f}\int_{V_f}a\,dV. \tag{4}$$

The last two terms in equation (2) include two coefficients related to the linear and nonlinear drag forces of the flow at the fluid-solid interface, α and β (respectively). They appear after applying a modified Forchheimer closure model for unsteady conditions [*Liu et al*., 1999] in order to solve the inter facial momentum transfer terms. Both coefficients need to be determined numerically as they rely heavily on the flow and porous media characteristics to be modeled (see section 3.2). In the clear-fluid region, i.e., $\phi=1$ and $C_A=0$, the VARANS equations become identical to the typical RANS equations. The volume of fluid (VOF) method of *Hirt and Nichols* [1981] is used to track the free surface and the finite difference two-step projection method [*Chorin*, 1969] is adopted to solve the governing equations. *Lin and Liu* [1998a,b] provide a full description of the COBRAS model and additional works by *Liu et al*. [1999] and *Hsu et al*. [2002] elaborate on the implementation of the porous media and related physics. Hence, interested readers are referred to the aforementioned studies for detailed information.

3.2. Numerical Implementation and Model Calibration

The numerical setup follows the the experimental layout as described in section 2 (Figure 1a). The coordinate system has its origin at the intersection of the still water and the bed slope. The spatial coordinates are defined in a bed-parallel (x) and bed-orthogonal (z) reference system, with positive x increasing upslope (onshore) and z increasing above the bed. The release of the dam break is produced by gravity at $t=0$ s and hence, the gate motion is not modeled.

The computational grid is irregular with a refined subzone around the fluid-porous interface (Figures 1b and 1c) along the surf-to-swash transition until the landward end of the beach face (from $x=-3.41$ m until $x=4.01$ m and from $z=-0.05$ m until $z=0.25$ m). The minimum grid cell dimensions in this finer region are $\Delta x=\Delta z=0.003$ m. Thus, 174 vertical grid cells resolve the fluid-porous interface corresponding to the first 0.25 m of water above the bed. The entire computational domain is composed of 863,604 cells. The simulation

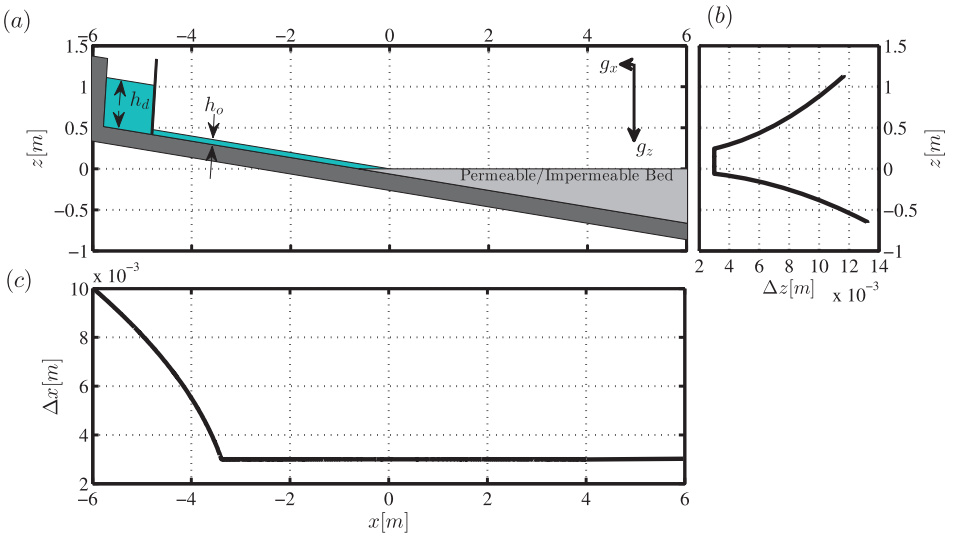

Figure 1. (a) Numerical set up in bed-parallel and bed-orthogonal coordinates, and initial conditions for the liquid phase. h_d is the water depth inside the reservoir and h_o outside the reservoir. The initial still water level of the subsurface flow inside the porous bed is also defined by h_o. (b) Grid cell length variation in the bed-orthogonal direction z. (c) Grid cell length variation in the bed-parallel direction x.

time is set at 12.1 s based on the duration of the laboratory experiments. The computation times for a single simulation range from approximately 4–18 h for the impermeable and permeable cases, respectively, using an Intel Xeon 2.53 GHz (6GB RAM) computer.

The mean flow is described by the zero stress condition and a zero gradient condition for both k and ϵ [*Lin and Liu*, 1998b] at the free surface boundary. For the impermeable case, the logarithmic law for u_x is prescribed at the bottom and it extends until the first grid point above the bed, while u_z is zero at bed. Both u_x and u_z at higher grid points in the water column are solved numerically [*Lin and Liu*, 1998a; *Torres-Freyermuth et al.*, 2013]. The bed-parallel velocity at half the first grid point above bed ($u_{ab/2}$) is then used to determine the friction velocity, u_*, as,

$$u_* = \frac{\kappa \overline{u_{ab/2}}}{\ln\left(\frac{30 z_{ab/2}}{K_s}\right)}, \tag{5}$$

where $z_{ab/2}$ is the z distance from the bed to the middle of the overlying first grid cell, $\kappa = 0.4$ is the von Karman constant, and K_s is the equivalent roughness height. The kinematic viscosity and turbulent eddy viscosity, ν_k, are used to determine the shear stress given by,

$$\tau_{xz} = \rho(\nu + \nu_k)\left(\frac{\partial \overline{u_x}}{\partial z} + \frac{\partial \overline{u_z}}{\partial x}\right). \tag{6}$$

There are different expressions to determine the value of K_s that range from d_{65} to $5.1d_{84}$ (for an overview refer to *Sleath* [1984] and *Puleo and Holland* [2001]). In the present study, $K_s = 1.2d_{50}$ is selected by optimizing the model skill for the instantaneous water depth evolution (h), the depth-averaged bed-parallel velocity (U_x), near bed ($z = 0.010$ m) k, and shoreline motion (S). The instantaneous shoreline, is defined as the most landward location where water intersects the second grid node (i.e., $z = 0.006$ m), whereas the measured shoreline refers to the LIF readings extracted at $z = 0.005$ m. No interpolation techniques between grid cells are employed for the predicted shoreline. Hence, the related differences in the estimation of S are accepted and included in the skill analysis. The model skill value is defined as [*Willmott et al.*, 1985],

$$\theta_{skill} = 1 - \left[\frac{\sum_{t_{ini}}^{t_{end}} \left(\theta_{pred,t} - \theta_{meas,t}\right)^2}{\sum_{t_{ini}}^{t_{end}} \left(|\theta_{pred,t} - \overline{\theta_{meas,t_{ini:end}}}| + |\theta_{meas,t} - \overline{\theta_{meas,t_{ini:end}}}|\right)^2}\right], \tag{7}$$

for a predicted (θ_{pred}) and measured (θ_{meas}) quantity, over the time period from the first measurement (t_{ini}) to the last (t_{end}). The model skill ranges from 0 (complete disagreement) to 1 (perfect agreement) and it is

Table 1. Simulated Impermeable Tests, K_s Values Used, and Averaged Model Skill Values of Water Depth Evolution (h_{skill}), Depth-Averaged Bed-Parallel Velocity ($u_{x_{skill}}$), Near Bed Turbulent Kinetic Energy (k_{skill}), and Shoreline Motion (S_{skill})

Test	K_s (m)	h_{skill}	$u_{x_{skill}}$	k_{skill}	S_{skill}
1	$0.5d_{50}$	0.85	0.98	0.79	0.95
2	$0.8d_{50}$	0.85	0.99	0.77	0.97
3	$1.0d_{50}$	0.86	0.99	0.76	0.97
4	$1.2d_{50}$	0.91	0.97	0.74	0.99
5	$1.6d_{50}$	0.87	0.99	0.73	0.97
6	$2.0d_{50}$	0.90	0.98	0.71	0.98
7	$2.4d_{50}$	0.93	0.97	0.70	0.98
8	$3.0d_{50}$	0.97	0.92	0.69	0.99

chosen as it is nondimensional, posing advantages for assessment across variables with different units [*Liu et al*., 2009]. Table 1 contains the different values of K_s tested and the corresponding model scores obtained after averaging the individual model skill values for the swash zone locations where experimental measurements are available.

The first calibration step refers to the determination of an optimal value for the total porosity in the context of the numerical formulation, as the model is highly sensitive to such parameter. *Steenhauer et al*. [2011] reported values of 2.5×10^{-8} m s^{-1} and 0.3 for the intrinsic permeability (k_p) and ϕ respectively, which hold for the gravel material used by *Kikkert et al*. [2012, 2013]. However, in this study a value of $\phi = 0.2$ yielded a better agreement with respect to measured data. The second calibration step of the model in the presence of the permeable bed requires the determination of α and β coefficients in equation (2). Some guidance in the prospective values of α and β exists in the literature [e.g., *Liu et al*., 1999; *Hsu et al*., 2002; *Lara et al*., 2006a, 2008]. However, most of the previous studies were focused on wave-structure interactions with porous elements in the range of 0.01–0.5 m. Therefore, here the selection of appropriate values is based on the model skill as defined by equation (7). Table 2 synthetizes the number of simulations performed and the range of the values in which α and β were systematically varied for each tested porosity. The resulting model skill values are reported after averaging the individual model skill values at the PIV/LIF swash zone measurement locations.

4. Model-Data Comparison

Torres-Freyermuth et al. [2013] validated the numerical model with the data set of *O'Donoghue et al*. [2010], consisting of dam break-driven swash over impermeable beds. In the present study, the model is further validated with the ensemble-averaged data of *Kikkert et al*. [2012, 2013], including the permeability of the bed. An additional measure to evaluate the model performance is obtained using the root-mean-squared error (RMSE), given by

$$RMSE = \sqrt{\frac{\sum_{t_{ini}}^{t_{end}} \left(\theta_{meas,t} - \theta_{pred,t}\right)^2}{n}}, \tag{8}$$

where n is the total number of time steps between t_{ini} and t_{end}.

Table 3 presents the RMSE for the water depth, depth-average velocity, and near bed turbulent kinetic energy at the different swash locations. The predicted and measured instantaneous shoreline position are in good agreement (see Figure 2). The computed RMSE values are 0.16 m and 0.14 m for the impermeable and permeable cases, corresponding to differences of 1.59 % and 2.04 % with respect to data. Thus, the numerical model is able to reproduce the overall shoreline motion for both types of beaches. The numerical model predict the decrease in the run up distance and the slower retreat of the shoreline motion, that results in a more asymmetric swash event for the permeable beach. For both cases, there is a slight temporal lag of 0.2 s during the initial uprush motion, between 1.8 s and 3 s, that is partly related to the gate motion that was not incorporated in the numerical model. Another possible source of error may be due to the air phase that is not resolved by the numerical model. Under the adopted scheme, the air bubbles are

Table 2. Summary of Simulated Permeable Tests, α and β Values, and Resulting Averaged Model Skill Values

Tests	ϕ	A	β	h_{skill}	$u_{x_{skill}}$	k_{skill}	S_{skill}
35	0.3	200–1	1.1–0.2	0.85–0.88	0.93–0.97	0.49–0.66	0.95–0.97
20	0.2	200–10	1.1–0.2	0.81–0.91	0.79–0.97	0.34–0.64	0.90–0.99
1	0.2	10	0.1	0.96	0.98	0.64	0.99
6	0.1	200–50	0.2–0.1	0.73–0.78	0.67–0.77	0.39–0.43	0.86–0.92

Table 3. Maximum Measured Magnitudes (*max*) and Model Root-Mean-Squared Errors (RMSE) for the Water Depth Evolution (h), Depth-Averaged Bed-Parallel Velocity (U_x), and Near Bed Turbulent Kinetic Energy (k) at Each Swash Location (x)

x (m)	h_{max} (m)	h_{RMSE} (m)	$U_{x_{max}}$ (m^2 s^{-1})	$U_{x_{RMSE}}$ (m^2 s^{-1})	k_{max} (m^2 s^{-2})	k_{RMSE} (m^2 s^{-2})
Impermeable						
0.072	0.172	0.017	1.526	0.106	0.071	0.009
0.772	0.119	0.011	2.157	0.081	0.060	0.014
1.567	0.089	0.009	2.057	0.072	0.505	0.021
2.377	0.060	0.007	1.611	0.077	0.318	0.014
3.177	0.038	0.008	1.001	0.142	0.271	0.010
Permeable						
0.072	0.172	0.010	1.585	0.080	0.055	0.008
0.772	0.128	0.007	1.980	0.070	0.119	0.010
1.567	0.069	0.009	1.845	0.126	0.203	0.007
2.377	0.033	0.008	1.479	0.206	0.372	0.041
3.177						

expelled into the bore tip and larger TKE may be induced [*Lin and Liu*, 1998b]. Thus, the small-scale details of the turbulent uprush bore front between the experimental and simulated swash flows are not likely to be equivalent. The run up distances are well-predicted, with maximum differences of 0.05 m and 0.04 m for the impermeable and permeable case, respectively. Moreover, the temporal lag by the time of the initial shoreline retreat is less than 0.1 s and 0.2 s for each corresponding case. At the end of the backwash phase (i.e., $t \sim 9$ s), a residual film of water, one grid point deep, remains attached to the bed in both cases. *Antuono et al.* [2011] concluded that the use a quadratic type frictional law (e.g., Chezy frictional terms) in NSWE-type computations implies that the only possible analytic solution for the shoreline motion is nonreceding. Moreover, the residual water layer has been reported in previous studies of swash-zone hydrodynamics based on RANS models [e.g., *Mory et al.*, 2011; *Desombre et al.*, 2013] and its appearance is not clearly understood. Therefore, further investigation should be devoted in RANS numerical models in order to be able to clarify this issue. However, a negligible effect in swash zone dynamics is observed consistent with previous studies [e.g., *Antuono et al.*, 2011].

Instantaneous h comparisons at the measurement locations (Figure 3, top) show a reasonable agreement, denoted by RMSE values, that on average represent less than 13% of the maximum measured values (h_{max}). In general, the asymmetric nature of the h evolution is reproduced by the numerical model, with rapid h increments during uprush, and longer duration for the backwash h reductions. Moreover, the predicted h asymmetry decreases in the landward direction. Some model over-prediction exists around flow reversal when h_{max} occurs. Nonetheless, the largest differences in h at $x = 2.37$ m (Figure 3c, top) are 0.009 m and 0.005 m for the impermeable and permeable cases, respectively. These differences span 1–3 grid points only. The most noticeable feature is the h lag during bore arrival at the landward-most location for the permeable case (Figure 3d, top). This temporal lag suggests a slight over-prediction in water loss at the fluid-porous interface since more fluid is required to saturate the subsurface as the bore travels along the sloping beach. This loss could be compensated by altering the values used for the fluid-porous interface. However, both the α and β coefficients were calibrated (section 3.2) for improving the overall model performance rather than solely the water depth estimation.

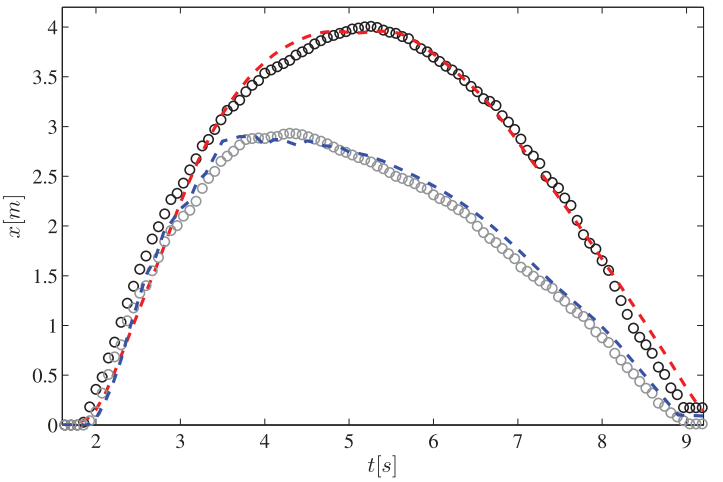

Figure 2. Shoreline motion time series for the measured-impermeable (open black circles), measured-permeable (open gray circles), predicted-impermeable (red dashed line), and predicted-permeable (blue dashed line) gravel beaches.

The model-data comparison of the depth-averaged velocity (i.e., U_x) at the evaluated locations

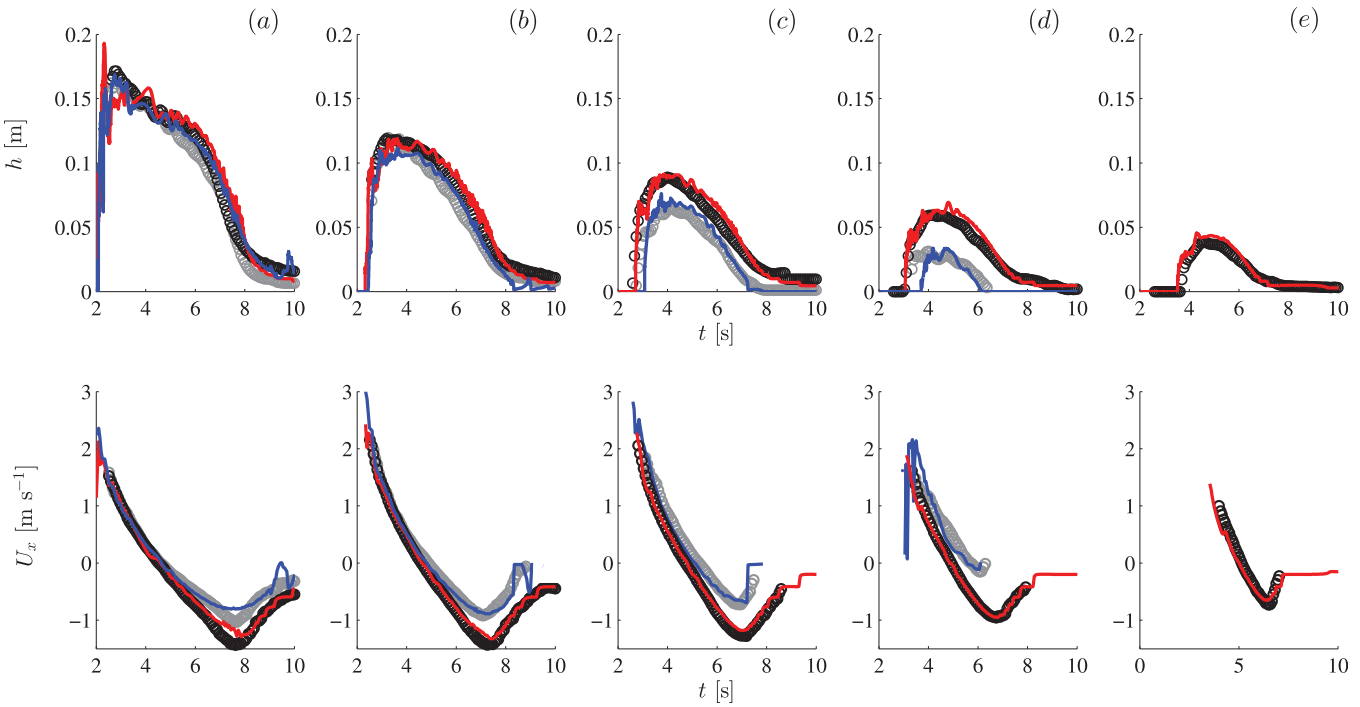

Figure 3. (top) Water depth and (bottom) depth-averaged bed-parallel velocity time series for the measured-impermeable (open black circles), measured-permeable (open gray circles), predicted-impermeable (red line), and predicted-permeable (blue line) gravel beaches at: (a) $x = 0.072$ m, (b) 0.772 m, (c) 1.567 m, (d) 2.37 m, and (e) 3.177 m swash zone measurement locations.

(Figure 3, bottom) yields RMSE values ranging from 0.07 to 0.14 ms^{-1} and from 0.07 to 0.21 ms^{-1} for the impermeable and permeable cases (see Table 3), respectively. These values represent an overall difference range from 3.5 to 14% for both cases, highlighting the close agreement between predictions and measurements. Again, the model predicts accurately the asymmetry between the (larger) uprush and backwash bed-parallel velocities across the swash zone. The higher predicted velocities ($U_x \geq 1.5$ ms^{-1}) occur during the initial uprush when the incident bore crosses a particular fixed position with large momentum flux gradients and high air bubble content. Thus, it is anticipated that for any given instance during the uprush phase, the magnitude of U_x is always larger for the permeable case than for the impermeable case for both predicted and measured data. The numerical model successfully predicts the reduction in U_x across the swash zone locations due to the increased water loss in the landward direction. The largest deviations for the model occur at the seaward location in the late backwash phase when the flow reaches maximum offshore velocity (e.g., see Figure 3a, bottom). This may be related to limitations in the boundary condition as the bottom roughness is kept constant [*Torres-Freyermuth et al.*, 2013]. Another related drawback is observed during the late backwash phase (i.e., $t \geq 8$ s) at the landwardmost locations (e.g., Figures 3a and 3b, bottom) as the residual flow from exfiltration is hindered. Nonetheless, limitations are not evident at landward locations (Figures 3b–3e, bottom), where the model and measured bed-parallel velocities are in good agreement.

In Figure 4, the model is compared against time series of the TKE at 0.009 m above the bed. The model predictions are consistent for both cases, with a slight TKE reduction in the permeable case related to the suction of turbulence into the bed. This effect is enhanced in the landward direction for both measured and predicted TKE values. The numerical model also successfully captures the cumulative effect of the backwash phase reduction [*Kikkert et al.*, 2013]. As a general overview, the differences between reported k_{RMSE} and k_{max} result in 9.4 % and 9.8 % for the (corresponding) impermeable and permeable cases after being averaged across all the swash locations.

On the other hand, the numerical model is qualitatively tested for simulating near bed dynamics induced by nonbreaking waves propagating over a porous bed. *Corvaro et al.* [2014] investigated the influence of in/out flows on nearbed vortical patterns, TKE structure, and fluctuations around the mean flow velocity due

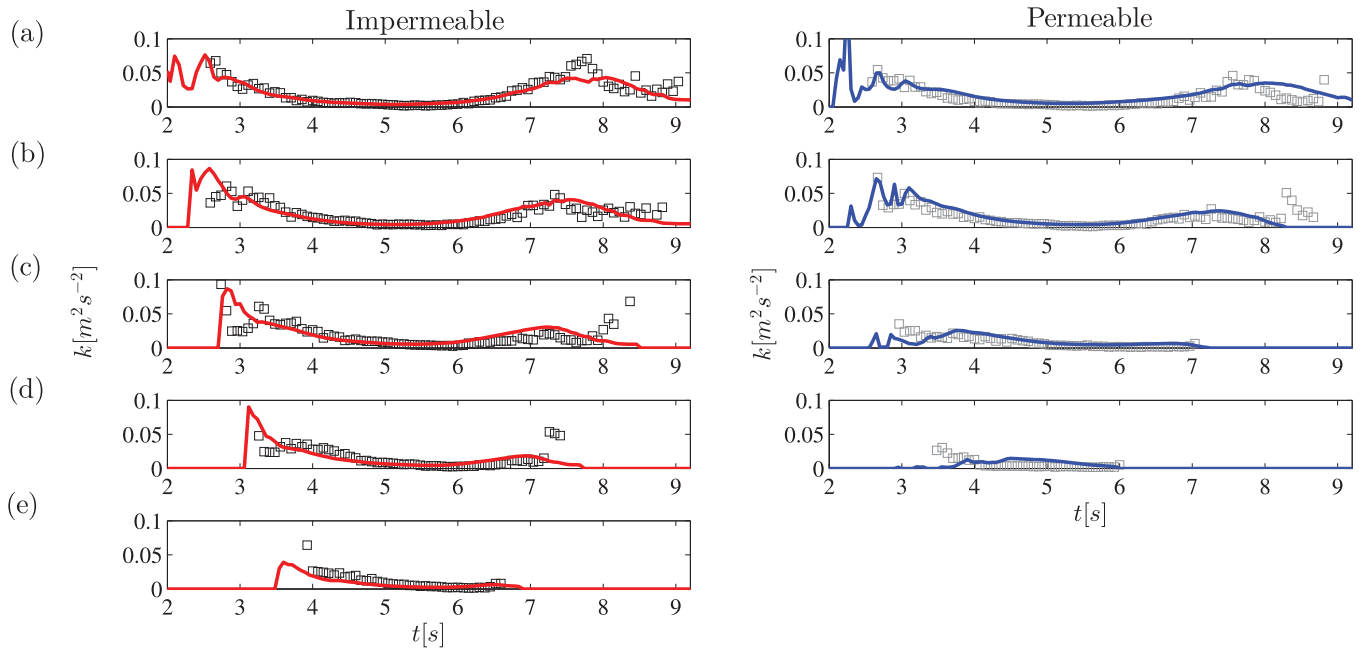

Figure 4. Near bed ($z = 0.009$ m) turbulent kinetic energy time series for the (left) impermeable and (right) permeable gravel beaches. Measured-impermeable (black open squares), measured-permeable (gray open squares), predicted-impermeable (red dashed line), and predicted-permeable (blue dashed line) time series are shown at (a) $x = 0.072$ m, (b) 0.772 m, (c) 1.567 m, (d) 2.37 m, and (e) 3.177 m, swash zone locations.

to coherent structures around the porous bed interface under the action of nonbreaking waves. Following the study by *Corvaro et al*. [2014], the VARANS model is implemented with similar boundary ($d_{50} = 0.036$ m; $\phi = 0.29$) and forcing ($H = 0.10$ m and $T = 2$ s) conditions. Figure 5 shows the bed-parallel (u_x) and bed-orthogonal (u_z) velocity components at two different near bed elevations, along one wave length (Figure 5a). Consistent with *Corvaro et al*. [2014] observations (Figures 5a1–5c1), the numerical model predicts fluctuations (Figures 5b2–5c2) around the mean flow driven by local pressure gradients under such oscillatory flow conditions. These fluctuations are described in *Corvaro et al*. [2014] as standing vortices that induce large scale modulations around the mean flow velocity while they propagate from one interstitial space to the next one in the local direction of the flow. This is supported by the range of the fluctuations around u_x and u_z that are phase dependent and more dominant at the top of the porous elements that characterize the bed interface (Figure 5c). The numerical results suggest that the VARANS model is able to reproduce the generation, physical length and evolution of the macro vortices, and related modulations in the near bed velocity signals. Furthermore, the qualitative agreement with *Corvaro et al*. [2014] observations also comprises the spatial gradients of near bed vorticity and local Reynolds shear stress (not shown).

5. Results

The model-data comparisons suggest that the VARANS k-ϵ numerical scheme is capable of simulating the transient nature of near bed properties from dam break driven flows [e.g., *Kikkert et al*., 2012, 2013] and the fundamental properties characterizing suction/injection events under oscillatory flow [e.g., *Corvaro et al*., 2014]. Therefore, the numerical model is further employed to investigate the influence of beach permeability and porosity on BL dynamics inside the swash zone. Normalized space and time coordinates are adopted in an effort to allow comparisons between cases and between locations across the area of interest. The time dimension is normalized as,

$$t' = \frac{t - t_a}{D}, \tag{9}$$

where $D = t_f - t_a$ is the event duration at any bed-parallel location inside the swash zone, defined by the instances during which the second grid cell above the bed (at $z = 0.006$ m) becomes initially wet due to the bore arrival (t_a), and when it becomes dry at the end of the backwash phase (t_f), and hence t' ranges from 0

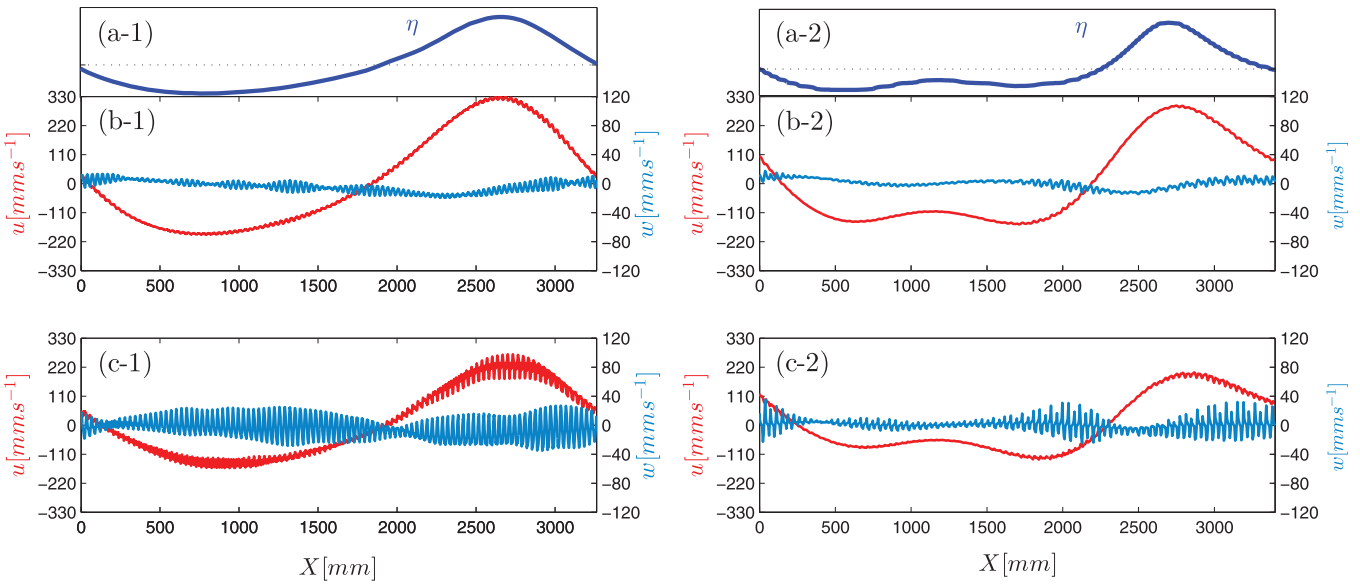

Figure 5. Dimensional mean velocity components over a one wave spatial length (Plots 1: *Corvaro et al.* [2014]; Plots 2: VARANS model). (a) Spatial wave length of the free-surface elevation η and (b, c) mean velocity dimensional components, u_x (in red) and u_z (in light blue), at two different elevations (b: $z \approx 0.01$ m; c: $z \approx 0.001$ m) above the top layer of the porous bed elements.

to 1. Then, each bed-parallel location is defined in terms of the maximum run up distance (L) as $x' = \frac{x}{L}$. The normalization in space is also enforced in the bed-orthogonal direction relative to the maximum water depth (h_{max}) at each normalized bed-parallel location x' as,

$$z' = \frac{z}{h_{max}} \tag{10}$$

5.1. Flow Velocity Structure

The time stack of the bed-parallel velocity u_x at $z = 0.009$ m above the bed for the entire swash event is shown in Figure 6a for both cases. The asymmetry of the swash event for the permeable case (Figure 6a, right) is more pronounced owing to the larger uprush and smaller backwash u_x velocities with respect to the impermeable case. At the most landward locations ($x' > 0.75$) the active region of infiltration is highlighted as the sudden transition from high positive to near zero u_x magnitudes. Moreover, the backwash duration is reduced in the landward direction until this phase is nonexistent at locations $x' > 0.8$ as previously suggested by *Steenhauer et al.* [2012a]. The u_x vertical distribution at the four x' locations (indicated by the black dashed lines in Figure 6a) is provided in Figures 6b–6e. Higher landward-directed (positive) velocities ($u_x \geq 1$ ms^{-1}) result during the initial uprush phase ($t' > 0.2$), that distribute from middle to maximum depths ($z' \geq 0.4$), for both cases and roughly at all locations. The uprush phase differences between permeable and impermeable cases relate to the near bed u_x structure in which the infiltration dominates over boundary layer development (Figures 6a–6d) [*Kikkert et al.*, 2013]. Higher near bed u_x values and more depth-uniformity in the u_x structure is found for the permeable case and in the landward direction (e.g., Figures 6c–6e). Thus, the thinning of the BL is dominant during uprush. Another relevant difference refers to the relative backwash phase duration and u_x backwash magnitudes. The permeable case has lower seaward-directed u_x magnitudes due to the reduced run up distance (e.g., Figure 2) that decreases the mass and momentum of the backwash flow. As a consequence, the near bed u_x structure is also more depth uniform during late backwash. In addition, the infiltration of water clearly enhances an uprush phase lead and subsequent decrease in the backwash duration. For instance, at the most landward location ($x' = 0.76$, Figure 6e) the flow reversal occurs at $t' = 0.41$ and $t' = 0.62$ for the impermeable and permeable cases respectively (implying an uprush phase lead of $t' = 0.21$).

5.2. Turbulence Balance

The spatial gradients of the turbulence field for both cases are provided in Figure 7a by means of the near bed turbulent kinetic energy evolution. Maximum values of TKE exceeding 0.08 m^{-2} s^{-2} are found during

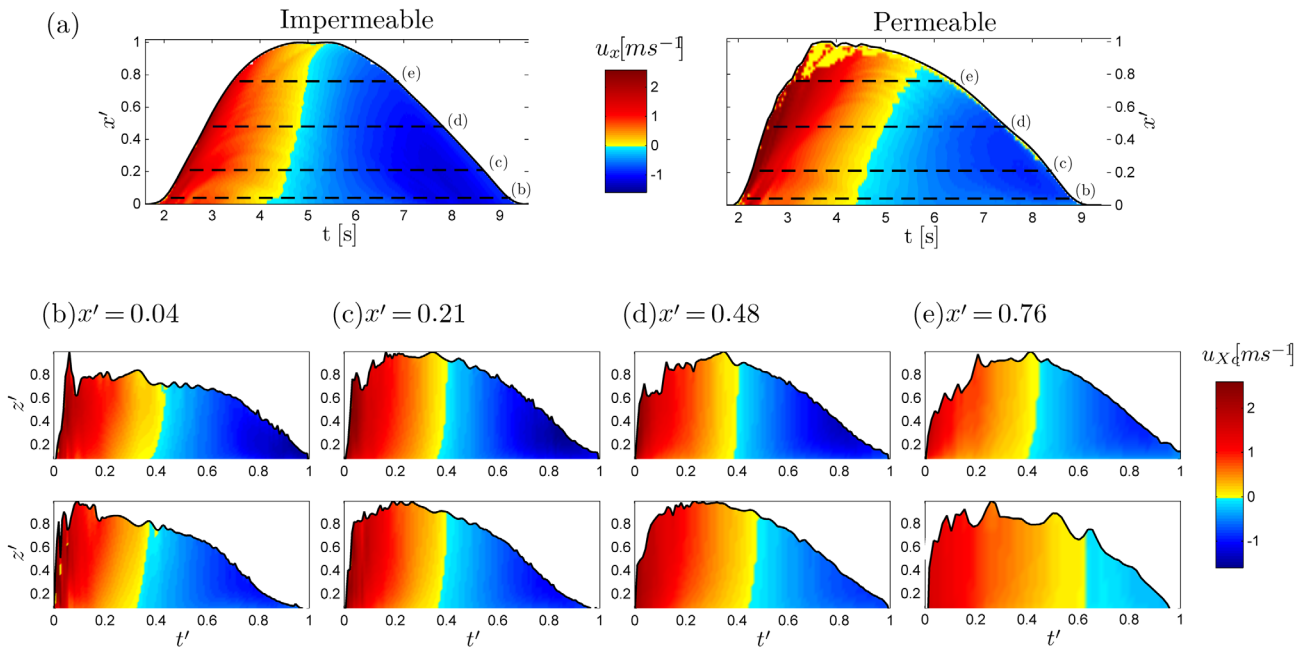

Figure 6. (a) Time stack of u_x at $z = 0.009$ m across the swash zone for the impermeable and permeable case. Black dashed lines indicate $x' = 0.04$, 0.21, 0.48, and 0.76 locations corresponding to Figures 6b–6e. (b–e) Time stacks of u_x structure at fixed selected x' locations in normalized time t' and bed-orthogonal z' frame of reference for the (top) impermeable and (bottom) permeable case.

the initial uprush phase, followed by turbulence decay during the late uprush and flow reversal, and bed-related turbulence during the backwash phase. In general, more energy transfer from the mean flow to the turbulence flow field is enhanced for the impermeable case given the larger TKE values during all phases. The infiltration of TKE is visible at landward locations (similar to Figure 6a), and diminished turbulence levels inside the surface flow during the backwash phase at middle to landward locations ($x' > 0.4$). The numerical model allows a close inspection of the turbulence field in order to evaluate the induced variations of each of the terms contained in the TKE balance due to the surface-subsurface exchange. The RANS k transport equation is expressed as

$$\underbrace{\frac{\partial k}{\partial t}}_{\text{I}} = \underbrace{-\overline{u_j}\left(\frac{\partial k}{\partial x_i}+\frac{\partial k}{\partial x_j}\right)}_{\text{II}} \underbrace{-\frac{\partial}{\partial x_j}\left[\left(\frac{v_t}{\sigma_k}+v\right)\frac{\partial k}{\partial x_j}\right]}_{\text{III}} \underbrace{+\overline{u_i' u_j'}\frac{\partial u_i'}{\partial x_j}}_{\text{IV}} \underbrace{-2\nu S_{ij}S_{ij}}_{\text{V}}, \tag{11}$$

where $S_{ij} = \frac{1}{2}\left(\frac{\partial u_i'}{\partial x_j}+\frac{\partial u_j'}{\partial x_i}\right)$ is the fluctuating strain rate tensor, $v_t = C_\mu \frac{k^2}{\epsilon}$ is the eddy viscosity, C_μ is a coefficient that depends on the local strain rate [*Hsu et al.*, 2002], and $\sigma_k = 1$. The local time rate of change of TKE (I) is given by the advection of the mean flow (II), diffusive transport by the pressure and turbulent fluctuations (III), TKE production (IV), and dissipation (V) [*Pope*, 2000; *Sou et al.*, 2010].

The TKE advection (II) is active during the initial uprush phase ($t' \leq 0.3$) at the landward location (Figure 7b) and its contribution is weakened at the middle swash zone location (Figure 7c) for both impermeable and permeable cases. During the late backwash phase ($t' \geq 0.7$), this term is again important (after flow reversal TKE decay) for the impermeable case while it remains almost inactive for the permeable case. The diffusive transport TKE term refers to the local TKE spreading through the water column. Hence, this term indicates local TKE transfer from the surface to the subsurface flow (negative-signed) or subsurface to surface TKE transfer (positive-signed) when it is evaluated near a ventilated bed. Figures 7b-III and 7c-III indicate that the net TKE transfer after the bore arrival ($0.05 \leq t' \leq 0.7$) is followed by a sudden shift in sign toward the subsurface (i.e., suction of TKE) at both swash zone locations.

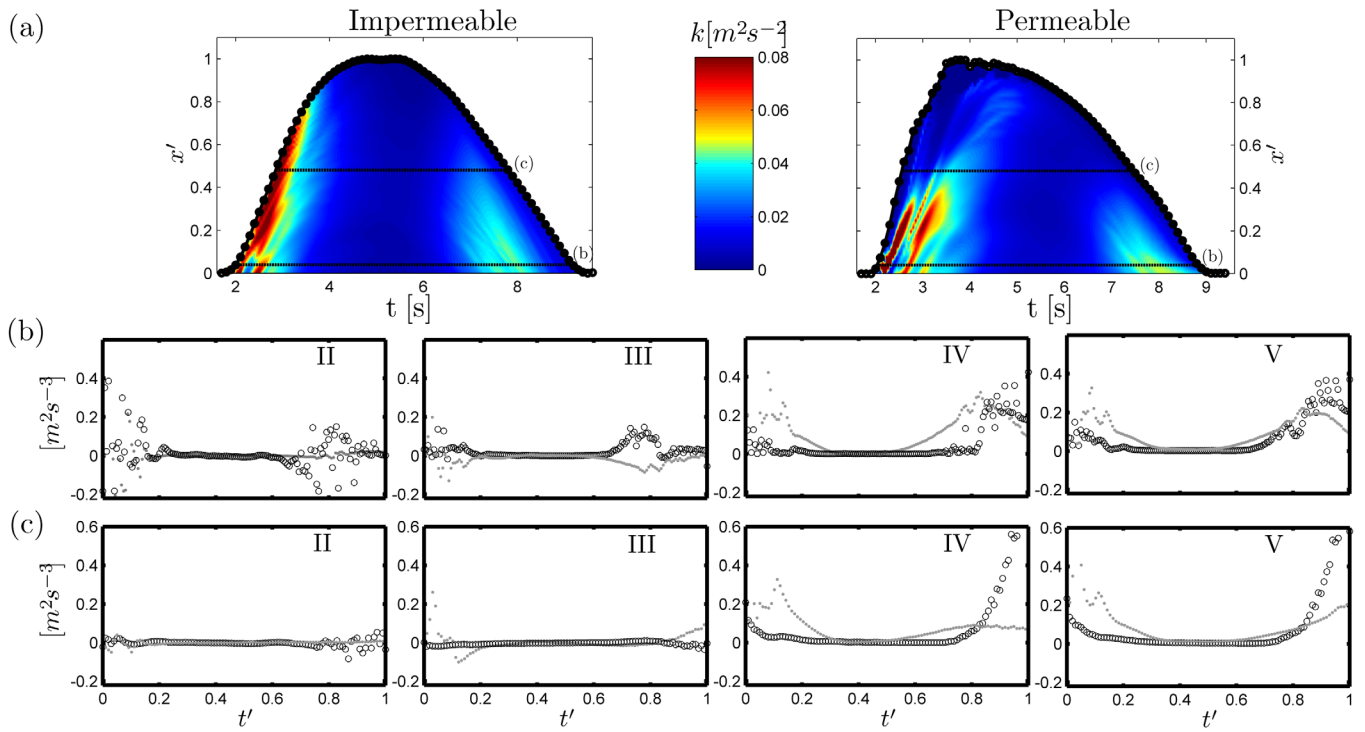

Figure 7. (a) Time stack of TKE at $z = 0.009$ m across the swash zone for the (left) impermeable and (right) permeable cases. Black dashed lines indicate $x' = 0.04$, and 0.48 locations corresponding to panels b and c. Evolution of the individual terms as expressed in the TKE balance (equation (11)) at $z' = 0.1$ for the impermeable (black symbols) and permeable (gray symbols) case: TKE convection (II), TKE diffusive transport (III); TKE production (IV), and TKE dissipation (V).

The surface to the subsurface TKE transfer reduces during the remaining uprush phase as the porous bed saturates. During the backwash and at the landward location (Figure 7c-III), the TKE transfer shift is from negative to positive, implying the spreading of TKE in the surface flow related to the exfiltration. In contrast, this term is positive during the majority of instances of high TKE for the impermeable case. The dominant TKE production (IV) and dissipation (V) terms relate the local turbulence generation due to friction forces into the TKE budget (e.g., shear stresses) and the sink of TKE in the form of internal energy. The terms are roughly in balance at both locations for the impermeable case. The increase in TKE production during the backwash phase suggests that there is sufficient time to develop a BL that counteracts the TKE dissipation. Hence, some TKE remains available for downslope advection in the backwash as indicated in the corresponding panel of term II.

The TKE production/dissipation balance for the permeable case is remarkably different. The uprush peak TKE production and TKE dissipation values of the permeable case with respect to the impermeable case are 3.2 and 2.2 times larger respectively at the seaward location (Figures 7b-IV and 7b-V). At the landward location (Figures 7c-IV and 7c-V), the corresponding values are 1.57 and 1.7 times larger for the permeable case. The same relative difference between cases during the backwash phase at the seaward location yields values that are 1.31 and 1.68 times lower for the permeable case. At the landward location the relative difference is 8.0 times lower (in TKE production), and 3.1 times lower (in TKE dissipation) for the permeable with respect to the impermeable case. These relative differences point out the influence of added/reduced shear and consequent TKE generation due to infiltrating/exfiltrating flows during the uprush/backwash phases. An important feature that results from the comparison is that the peaks in TKE production occur at the time of bore arrival during uprush, and at the time of maximum BL growth at the end of the backwash phase for the impermeable case. The corresponding peaks for the permeable case occur at the time of maximum infiltration during uprush, and by the time just before the exfiltration of water becomes dominant in the BL development.

5.3. Bed Shear Stress

The time stack of τ_{xz} at the impermeable/permeable bed are shown in Figure 8a. The results for the impermeable case are in general accordance with previous descriptions with maximum values related to the

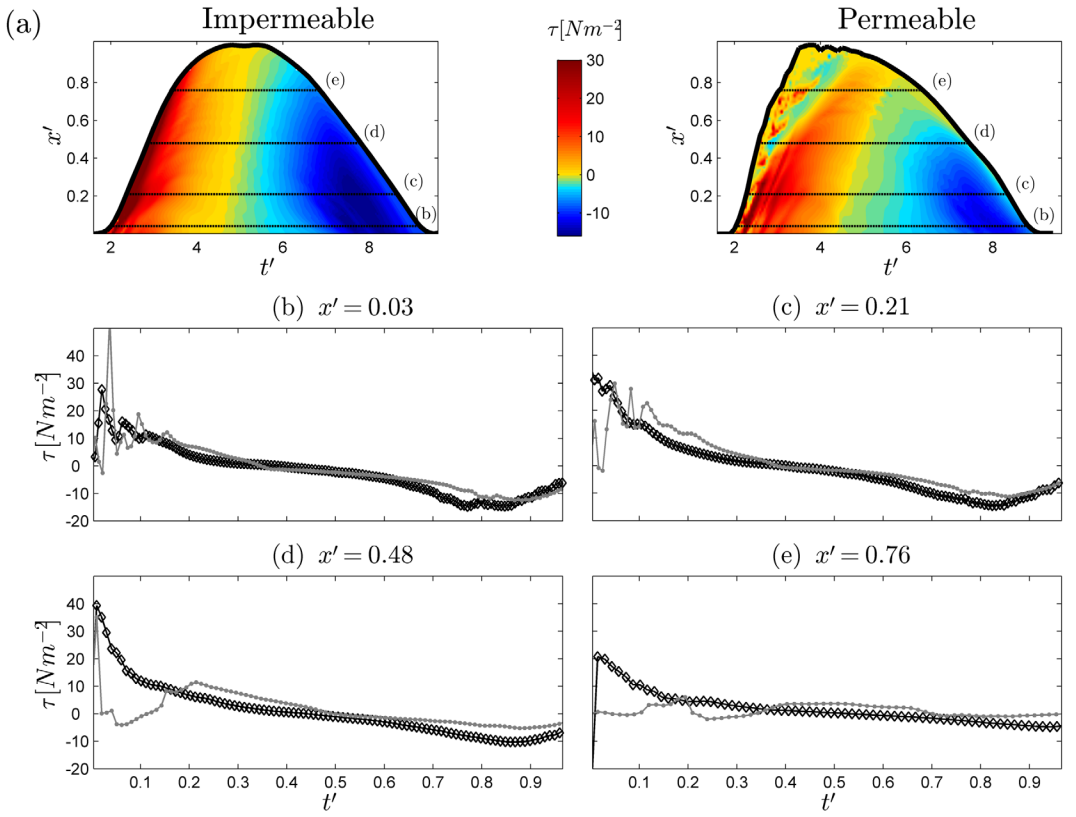

Figure 8. (a) Time stack of bed shear stress across the swash zone for the impermeable and permeable case. Black dashed lines indicate $x' = 0.04$, 0.21, 0.48, and 0.76 locations corresponding to Figures 8b–8e. (b–e) Evolution of τ_{xz} at fixed selected x' locations in normalized time t' and bed-orthogonal z' frame of reference for the (top) impermeable and (bottom) permeable case.

leading uprush flow [*Barnes et al.*, 2009] and decreasing values during the remaining uprush. During the backwash phase, τ_{xz} increases as the flow gains momentum and peaks before the end of the event. Indeed, the uprush τ_{xz} values are higher than during backwash but decrease to zero more rapidly while nonzero backwash τ_{xz} are present for a longer portion of the swash event [*O'Donoghue et al.*, 2010; *Kikkert et al.*, 2012; *Torres-Freyermuth et al.*, 2013]. The spatial average ratio of uprush to backwash τ_{xz} magnitudes across the entire swash zone is 3.8 for the peak bed shear stress and 1.6 for the mean values, consistent with the direct measurements of *Barnes et al.* [2009]. The spatial gradients of τ_{xz} is considerably different in the presence of bed ventilation. For the permeable case, the occurrence of maximum uprush τ_{xz} occurs at instances just after bore arrival and after sufficient time has passed to saturate the bed. The water at the leading edge is progressively affected by infiltration as the bore front propagates over the bed (thinning effect). Hence, the maximum τ_{xz} occurs at seaward swash zone locations ($x' < 0.2$) where the bore front is less influenced by infiltration. At landward swash zone locations ($x' > 0.4$), the infiltration of water becomes dominant and the τ_{xz} time history results in a sudden drop highlighting a region of low negative τ_{xz} where the infiltration mainly takes place (see Figures 8b–8e also). The τ_{xz} becomes positive again after the bed has reached saturation. The spatial τ_{xz} distribution during backwash is similar to the impermeable case but with lower overall magnitudes. For this case, the spatial average ratio of uprush to backwash values across the entire swash zone are 3.7 for maximum τ_{xz} and 2.6 for the mean τ_{xz}. Moreover, the peak uprush and backwash τ_{xz} magnitudes result in 80.8 N m^{-2} and 12.7 N m^{-2}, which compare to 77.8 N m^{-2} and 16.9 N m^{-2} for the impermeable case.

5.4. Mean Vorticity and Boundary Layer Thickness

Sou and Yeh [2011] investigated the ensemble-averaged vorticity field under plunging breakers in the surf and swash zones using PIV measurements. Their study validated the vorticity as an effective property to evaluate mechanisms that result from the combined action of pressure gradients, body forces at the water surface, and drag forces at the water-bed interface. Here the mean vorticity (ω) distribution is employed to

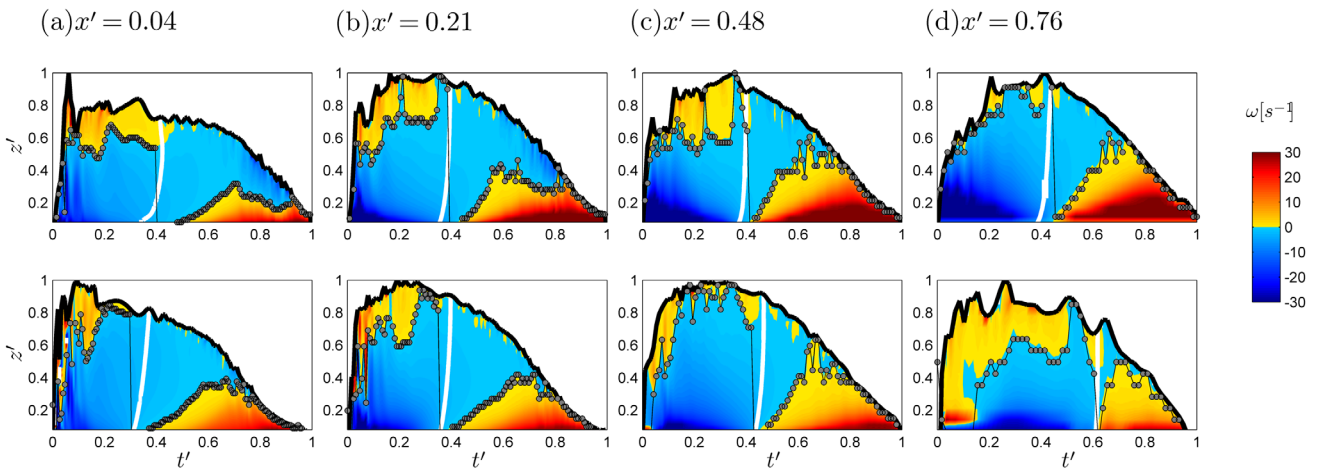

Figure 9. Time stack of ω structure in normalized t' and z' frame of reference at (a) $x' = 0.04$, (b) 0.21, (c) 0.48, and (d) 0.76 locations, for the (top) impermeable and (bottom) permeable case. The evolution of the BL thickness $\delta_{B\omega}$ (gray dotted line) is estimated by the first up-crossing of ω. The time of flow reversal (dashed white line) is shown also.

further evaluate the mean flow field variations due to the presence of the viscous and the free surface layers. The mean vorticity is estimated as,

$$\omega = \frac{\partial u_z}{\partial x} - \frac{\partial u_x}{\partial z} \tag{12}$$

Figure 9 shows time stacks of the ω field at different cross-slope locations ($x' = 0.04, 0.21, 0.48, 0.76$) as a function of normalized depth z'. Positive ω values correspond to counter clock wise (CCW) rotation, whereas negative ω corresponds to clock wise (CW) rotation. During the uprush motion, the ω is CCW at the surface and strongly CW at the bed denoting opposite forces acting on both boundaries. The direct comparison between the impermeable (Figure 9, top) and permeable (Figure 9, bottom) case reveals the different properties of the uprush flow. For instance, the horizontal straining induces CCW ω near the surface that tends to decrease toward land for the impermeable case, whereas it increases for the permeable case (see Figure 9d). Near the bed, the CW ω increases in magnitude in the landward direction for both impermeable and permeable cases during uprush. Conversely, strong bed-related CCW ω results from the zero shear condition (for the impermeable case), and momentum transfer during backwash. The first zero up-crossing of the bed-orthogonal ω profile from the bed level to the free surface at each t' is used as a proxy to quantify the time variant BL thickness ($\delta_{B\omega}$ from here on) as shown in 9a-d. The history of $\delta_{B\omega}$ shows that the BL is able to grow with less influence of surface induced forces for the permeable relative to the impermeable case. The backwash CCW ω is increasingly dominant in the landward direction and is more dominant for the impermeable case as it has more time to develop a BL.

From Figures 9a–9d, it is apparent that identifying the BL during the initial uprush is difficult due to bore-driven processes. The $\delta_{B\omega}$ develops instantaneously with the arrival of the bore and fluctuates underneath the water surface during the remaining uprush phase, suggesting that the BL is also modulated by the instabilities of the flow at the surface. The instabilities of the flow may be related to the horizontal strain after the bore arrival and subsequent small scale features such as the passage of the minibore [*Zhang and Liu*, 2008] that introduce additional CCW ω at the surface. Notably, $\delta_{B\omega}$ predicts that the BL becomes depth limited only before flow reversal for both cases, and in most swash zone locations (as in Figures 9c and 9d). At the most landward location and for the impermeable case (i.e., $x' = 0.76$), $\delta_{B\omega}$ is essentially depth limited for most of the uprush phase as the flow instabilities are progressively less and the flow propagates more homogeneous.

In contrast, for the permeable case the additional CCW vorticity at the surface is progressively more dominant in the landward direction. In addition, the suction of CW vorticity near the bed due to infiltration prevents the $\delta_{B\omega}$ to become depth limited (e.g., Figure 9d). The backwash phase allows a detailed inspection of the BL as its entire evolution is captured and is mainly bed-driven. The $\delta_{B\omega}$ grows freely with what appears

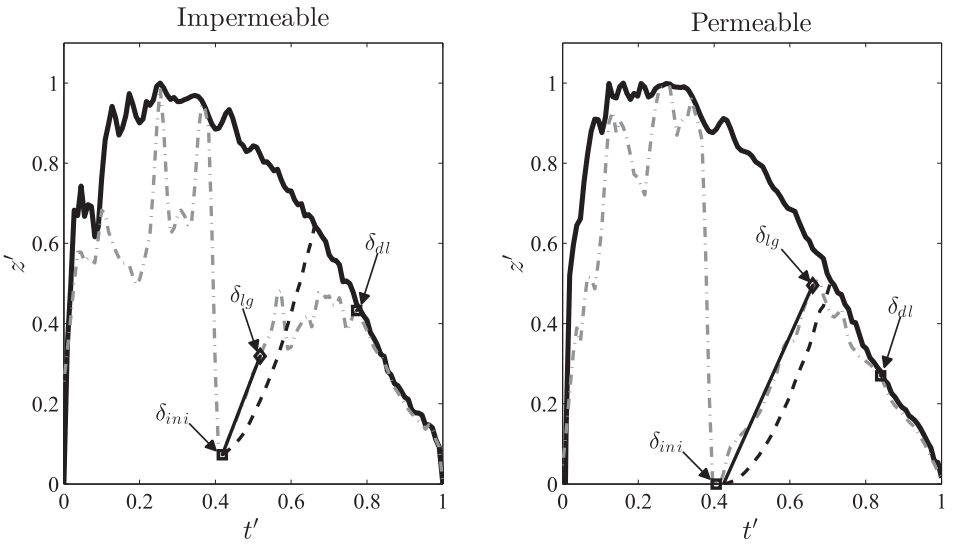

Figure 10. BL thickness $\delta_{B\omega}$ (gray dotted line) and water depth h (black line) evolution in normalized t' and normalized depth z'. The results are shown for the (left) impermeable/(right) permeable corresponding cases, and at $x' = 0.38$ location. The relative instance of initial BL development δ_{ini}, BL quasilinear growth limit δ_{lg}, and of depth limited growth δ_{dl} are highlighted.

to be a minimal impact from surface processes during the early backwash motion. Thus, the fact that the initial $\delta_{B\omega}$ evolution during the backwash behaves quasi-linear is highlighted and further analyzed.

5.5. Boundary Layer Growth Across the Swash Zone

Figure 10 shows the typical evolution of the $\delta_{B\omega}$ at $x' = 0.38$ as predicted by the zero up-crossing of ω, and it is used to exemplify the approach. Three distinctive instants during the backwash $\delta_{B\omega}$ evolution at each fixed x' are identified in order to estimate the range over which the BL quasi-linear growth occurs: (i) the minimum $\delta_{B\omega}$ after flow reversal (δ_{ini}) when the BL starts developing, (ii) the maximum $\delta_{B\omega}$ after δ_{ini} where the growth fits a linear trend in a least square sense (δ_{lg}), and (iii) the late backwash, during which $\delta_{B\omega}$ becomes depth-limited (δ_{dl}).

These temporal bounds are determined in the following steps: (1) δ_{ini} is easily identifiable by the minimum value of $\delta_{B\omega}$ from the time of flow reversal to 2/3 of the backwash phase duration. (2) We subtract $\delta_{B\omega}$ from the water depth (h') in the period between δ_{ini} and the end of the backwash. A shorter time window is defined by the instances (toward the end of the backwash) when the subtraction corresponds to values that are less than 0.05. Then, δ_{dl} is defined as the first time step (in the corresponding time window) when the third derivative of the subtraction is equal to zero (i.e., $\frac{\partial^3}{\partial t'^3}[h' - \delta_{B\omega}] = 0$). This implies that at least 3 consecutive time steps in the $\delta_{B\omega}$ time history are equal to or slightly smaller ($\Delta z' < 0.05$) than h', and have the same temporal variation as h'. (3) A linear fit between δ_{ini} and δ_{dl} is computed. If the correlation coefficient r^2 between $\delta_{B\omega}$ and the linear fit is less than 0.95 (with a 95% confidence level), the fit is rejected and a new fit is performed between δ_{ini} and $\delta_{B\omega}$ one time step before δ_{dl}. This step is repeated in an iterative process until a value of $r^2 \geq 0.95$ is obtained which defines δ_{lg}. Hence, the slope of the fit denotes the quasi-linear temporal growth of $\delta_{B\omega}$ as a function of time during the initial backwash phase. (4) Steps 1–3 are evaluated at every x' to obtain the initial backwash BL growth distribution across the swash zone (Figure 11). We note that the analysis is performed in the original temporal and depth coordinates (before normalizing) to obtain real estimates of BL growth rates. The x' normalized convention is retained since it is not used in the BL growth estimation, and as it allows the spatial comparison between cases.

The instances corresponding to δ_{ini}, δ_{lg}, and δ_{dl} across the swash zone are depicted in Figure 11. The spatial trend for δ_{ini} shows that the initial backwash BL growth occurs progressively at later times in the landward direction for both cases. Consequently, the time span between δ_{ini} and δ_{dl} is shortened at each sequential location in the landward direction and further emphasized for the permeable case (previously addressed as the uprush phase lead in Figure 6). At $x' > 0.84$ locations for the permeable case, the aforementioned analysis is hampered by the fact that the backwash phase is almost nonexistent. Figure 11 indicates that the time

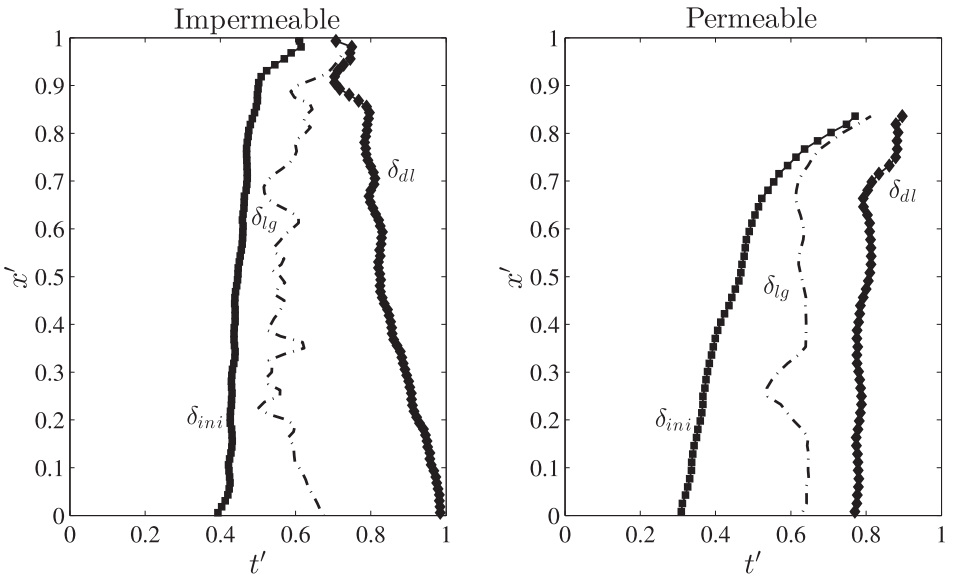

Figure 11. Relative instances of initial backwash $\delta_{B\omega}$ development δ_{ini} (black squares), BL quasilinear growth limit δ_{lg} (dash-dotted line) and of depth BL limited growth δ_{dl} (black diamonds) in normalized t' at all x' swash locations, for the (left) impermeable/(right) permeable cases. The period of quasi-linear BL is given by the time span from δ_{ini} to δ_{lg} during the backwash phase.

span of quasi-linear BL growth (between δ_{ini} and δ_{dl}) in the landward direction is progressively longer for the impermeable case, while the corresponding time span is shortened for the permeable case. Thus, the infiltration of water still occurs during the initial backwash at $0.78 < x' < 0.84$ and the quasi-linear $\delta_{B\omega}$ growth period is noticeably reduced. A rough estimate of the relative period of quasi-linear $\delta_{B\omega}$ growth with respect to the total backwash duration, results in a minimum 5% (at $x' = 0.68$) and maximum of 28% (at $x' = 0$) for the impermeable case. The corresponding range is from 2% (at the landward end) to 32% (at the seaward limit) of the total backwash duration for the permeable case. In summary, bed ventilation enhances the quasi-linear BL growth at the seaward and middle swash zone locations where the subsurface is expected to be saturated by the time of flow reversal. At landward locations, the infiltration of water still occurs during the initial backwash and the $\delta_{B\omega}$ growth deviates rapidly from a quasi-linear rate of growth.

6. Discussion

6.1. Suitability of Mean Vorticity as a Proxy for BL Thickness

In the present study, the BL thickness is determined by the zero up-crossing of ω. The validity of this assumption in relation to existing BL theory commonly applied to swash flows is addressed further. The spatial gradients of ω during an instance in the uprush ($t = 4.9$ s), and in the backwash phase ($t = 6.2$ s) are presented in Figure 12. For clarity, the frame of reference has been set to real (not rotated) coordinates (i.e., X and Z). The infiltration of CW and CCW ω during the corresponding uprush and backwash flows is successfully captured by the VARANS model, providing evidence of ω sinking into the bed. Some differences in relation to previous studies result from the fact that most descriptions are for oscillatory flow without wave breaking [e.g., *Corvaro et al*., 2014], or mainly focused on surf zone hydrodynamics [e.g., *Lin and Liu*, 1998b].

In the surf zone, ω maintains the same rotational direction as the overturning flow just below the free surface [*Lin and Liu*, 1998b]. Inside the swash zone, the bore front propagates initially over a dry bed and ω is more influenced by bed-related shear rather than surface properties. However, there are sub regions of alternating CCW and CW ω near the surface indicating divergence/convergence patterns. *Sou and Yeh* [2011] also described advected CCW ω at the surface inside the swash zone during the uprush phase which was related to wave-swash interactions in the inner surf zone. Here in the absence of wave-swash interactions, it is shown that local mechanisms are able to generate similar divergence/convergence patterns. The momentum gradients that result from accelerating/decelerating portions of the flow lead to the formation of the flow divergence/convergence envelopes below the moving surface. These mechanisms at the surface, together with the

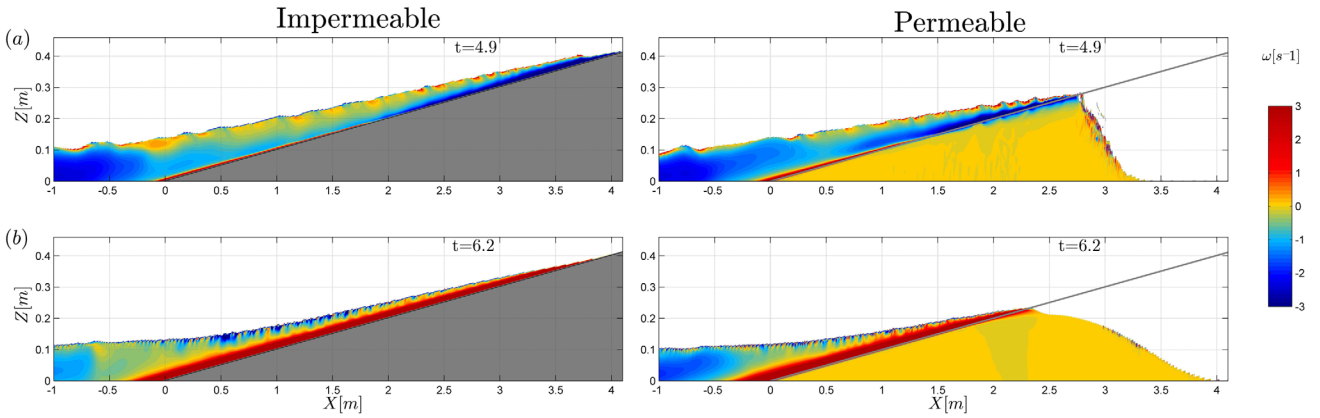

Figure 12. Mean vorticity ω distribution for the (left) impermeable and (right) permeable case in (real) *X*and *Z* spatial coordinates, during (a) t = 4.9, and (b) t = 6.2.

transfer of bed shear stress and sinking/injection of TKE due to infiltration/exfiltration, control the ω evolution inside the swash zone as the flow is shallow. Hence, they have an important role in modulating the BL growth.

The suitability of the $\delta_{B\omega}$ approach is investigated by alternatively estimating the BL thickness from the u_x structure and the log law approach for comparison. The BL thickness from the log law approach (δ_{Blog}) is obtained as the highest location in the z' direction where the fit between the logarithmic model and the u_x profile has a correlation coefficient (r^2) equal to or exceeding 0.95 [e.g., *Torres-Freyermuth et al.*, 2013]. The comparisons are presented in Figure 13 for the $X = 0.04$ swash zone location, where the u_x profiles at both beaches have smaller overall differences between each other. The BL thickness evolution is qualitatively similar using the two different methods, showing rapid uprush growth, decay around flow reversal, and backwash growth until limited by depth (consistent with *Barnes and Baldock* [2010] and *Briganti et al.* [2011]). However, some important differences are seen between the two approaches. The δ_{Blog} is almost depth-limited at all relative instances of the uprush phase (from $t' = 0.08$ to 0.32), whereas $\delta_{B\omega}$ is not predicted to be depth limited at any relative instance in any of the cases. The difference between methods is related to the horizontal straining of the flow that may induce a log type u_x structure which is not due to bed related shear stress [*Torres-Freyermuth et al.*, 2013]. For both cases, the δ_{Blog} around flow reversal (i.e., $t' = 0.36$) is under-predicted with

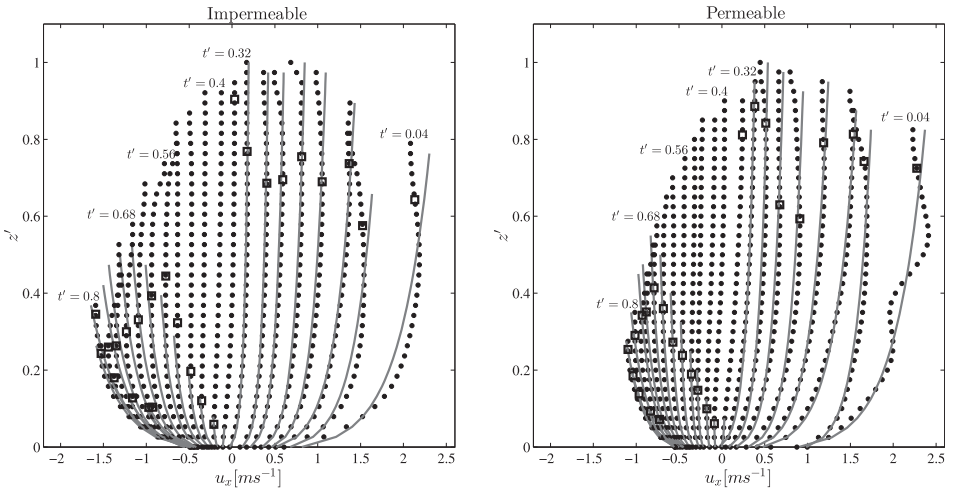

Figure 13. Bed-parallel velocity u_x profiles (black dots) at 1/25 fractions of the normalized t' swash cycle at $x' = 0.04$ location, for the impermeable and permeable case. The BL thickness is determined by the normalized depth z' at which a logarithmic distribution fits the u_x profile δ_{Blog} (gray solid line), and alternatively by the first zero up-crossing of mean vorticity $\delta_{B\omega}$ (black open squares). The results are presented in a normalized z' scale relative to the maximum water depth experienced during the entire swash cycle at that relative x' location.

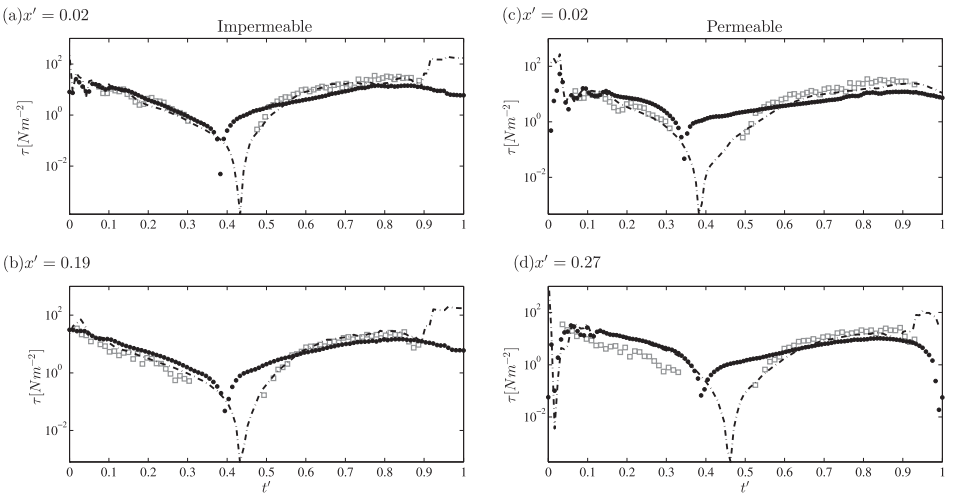

Figure 14. Time series of shear stress reported by *Kikkert et al*. [2012, 2013] (gray open squares), from the numerical output (black dots) using equation (6), and as predicted by the log law fit to the model predicted u_x structure (dash dotted line). The results are shown in the coordinate system adopted at: (a) $x' = 0.02$ and (b) $x' = 0.19$ for (left) the impermeable, and at (c) $x' = 0.02$ and (d) $x' = 0.027$ for (right) the permeable case. The selection of the x' reported locations is restricted to the existence of available measured data.

respect to $\delta_{B\omega}$, when the later predicts a maximum thickness just before the flow reversal. As expected, the logarithmic law fit is unable to represent the u_x with opposing directions near the bed and at the surface [e.g., *O'Donoghue et al*., 2010]. It is also shown that during the late backwash phase ($t' \geq 0.68$), the BL becomes depth limited at prior instances with the use of δ_{Blog}, suggesting a faster BL growth. Hence, the use of δ_{Blog} may lead to over/under predictions of the BL thickness during uprush/backwash. Another constraint of the δ_{Blog} approach is that it partly relies on the cutoff r^2 value used for its calculation.

6.2. Bed Shear Stress and Log Law

Bed shear stress estimates are discussed as a key quantity modulating the formation and progression of the BL. The bed shear stress based on the log law velocity structure as reported by *Kikkert et al*. [2012, 2013] and as obtained by the model with equation (6) are compared in Figure 14 (in normalized coordinates for consistency). The corresponding bed shear stress estimates differ mostly at the seaward most location where there is available data (i.e., $x' = 0.02$), with maximum observed differences of 6 N m^{-2} for the impermeable, and of 17 N m^{-2} for the permeable case. It is pointed out that the bed shear stress around bore arrival and late backwash phase in *Kikkert et al*. [2012, 2013] are not reported due to quality control and unsuitability of the log law during flow reversal (opposite directions of the flow). *O'Donoghue et al*. [2010] reported differences of $O(1)$ between direct measurements [*Barnes et al*., 2009] and log law derived bed shear stress, corresponding to the backwash phase. Meanwhile, *Torres-Freyermuth et al*. [2013] showed a better agreement to the *Barnes et al*. [2009] data during both, uprush and backwash phases, using the same numerical model and bed shear stress equation as the present study. Here in consistency, the maximum differences between the aforementioned approaches are found during the initial instants of the backwash phase. However, the observed differences with respect to data are noticeably reduced if the log law (as in *O'Donoghue et al*. [2010] and *Kikkert et al*. [2013]) is applied to the u_x structure from the model output (dashed dotted line in Figure 14). In this manner, it is demonstrated that the differences relate more to the method for estimating τ_{xz} rather than disparities in the u_x structure. Note that the bed shear stress magnitudes during bore arrival, flow reversal and end of the backwash phase are kept in Figure 14 to further illustrate the deviations of the log law with respect to equation (6).

6.3. Quasi-Linear BL Growth During Initial Backwash

An outcome of the analysis provided in section 5.5 is the estimation of the spatial distribution of the quasi-linear BL growth rate ($\frac{\Delta\delta_{B\omega}}{\Delta t}$) during the initial backwash phase. The growth rate between δ_{ini} and δ_{lg} at each fixed swash zone location is shown in Figure 15. The analysis shows that the initial backwash $\frac{\Delta\delta_{B\omega}}{\Delta t}$ is reduced at locations where the porous bed media has reached saturation, away from exfiltration and infiltration effects. For instance, at the seaward to middle swash zone locations ($0.1 \leq x < 0.45$) the flow

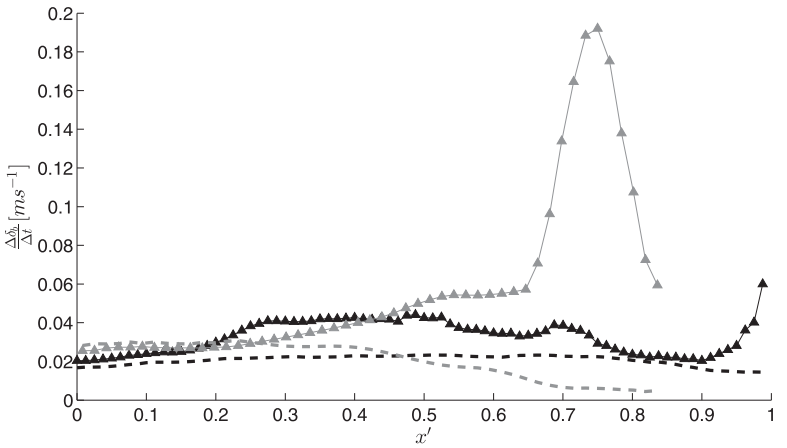

Figure 15. BL rate of growth at the initial backwash phase for the impermeable (black triangles) and permeable (gray triangles) case in normalized t' at all x' swash locations. The BL rate of growth as predicted by FPBL theory for a turbulent flow over a rough flat plate is also shown for each, impermeable (black dashed line) and permeable case (gray dashed line).

above the permeable bed possesses less momentum (reduced velocities, see Figures 3 and 6) and it is saturated by the time of the backwash phase (Figure 6a). Hence, the BL rate of growth is reduced for the permeable with respect to the impermeable case which in contrast, exhibits a faster backwash BL rate of growth. The most distinctive aspect is captured at middle to landward swash zone locations, where the backwash phase still exists for the permeable case (i.e., $0.45 \leq x < 0.84$). At the middle swash zone locations (i.e., $0.45 \leq x < 0.65$), the initial backwash phase occurs with simultaneous infiltration of water mass into the bed leading to larger bed shear stress under decreasing flow depths. Hence, the continuity effect [*Baldock and Nielsen*, 2010] is increasingly dominant [*Kikkert et al.*, 2013] and the BL develops more rapidly for the permeable case. At the most landward swash zone locations (i.e., $0.65 \leq x < 0.84$) the continuity effect is dominant, and the BL is largely modified during the initial instances of the backwash phase. The initial backwash $\frac{\Delta\delta_{B\omega}}{\Delta t}$ increases from 0.06 m s^{-1} (at $x = 0.65$) to 0.19 m s^{-1} (at $x = 0.75$), suggesting that the backwash BL becomes depth limited in very short periods of time. Additional assessment in the analysis is gained by applying fundamental turbulent flat plate BL theory (FPBL) commonly used to determine the BL evolution of swash zone flows [e.g., *Barnes and Baldock*, 2010]. Figure 15 shows the backwash $\frac{\Delta\delta_{B\omega}}{\Delta t}$ as predicted by the Prandtl and von Karman's FPBL momentum integral approach based on the 1/7 power velocity distribution law [*Schlichting and Gersten*, 2000]. As a general outcome, the FPBL theory predicts the spatial distribution of $\frac{\Delta\delta_{B\omega}}{\Delta t}$ within a factor of 2 at the seaward end of the swash zone. However, at the middle and landward swash zone portions of the flow, the $\frac{\Delta\delta_{B\omega}}{\Delta t}$ is not well-predicted; especially for the permeable bed with the dominant effects of infiltration. Hence, the applicability of the FPBL approach in the swash zone should be used with care when the flow presents sudden accelerations and significant infiltration, such as in natural coarse grained beaches.

7. Conclusion

A study of BL dynamics inside the swash zone for impermeable and permeable beds is performed using a 2-D VARANS numerical model. The numerical model is tested with dam break driven swash zone data [*Kikkert et al.*, 2012, 2013], showing good agreement given the model skills obtained. The main limitations refer to the permeable case as the air-induced pressure build-up inside the porous media is not accounted for in the model. However, typical computed relative errors are in the order of 2% for shoreline motion, 13% for instantaneous water depth, 14% for depth-averaged bed-parallel velocity and 10% for near bed turbulence. Hence, the numerical model is further employed to investigate the spatial gradients of flow properties at different phases and effects due to infiltration/exfiltration. The main dissimilarities of the surface flows between the permeable and impermeable beach are caused by a decrease in run up distance ($\sim$1.1 m), reduction in the surface water volume ($\sim$33%), and consequent reduction in momentum (differences in backwash velocities larger than 0.6 m s^{-1}).

The mean vorticity responds to momentum gradients that result from accelerating/decelerating portions of the flow below the moving surface, transfer of bed shear stress and sinking/injection of TKE due to infiltration/exfiltration. Hence, the zero up-crossing (from bed to surface) of vorticity in the swash zone leads to the quantification of the BL thickness. The BL develops instantaneously with the bore arrival. Shortly afterward, the BL is not depth limited but its thickness fluctuates and responds to surface instabilities of the flow that result from mini scale processes (i.e., minibore and horizontal straining). The BL reaches the free surface only before the flow reverses direction. Thus during uprush, the BL is modulated by the following mechanisms:

1. the infiltration of water that results in the progressive thinning of the bore front which is enhanced in the landward direction until the maximum run up distance.
2. the sinking of turbulence, identified by a shift in sign of the TKE diffusive transport term after the bore arrives at any particular swash zone location.
3. the magnitudes of maximum bed shear stress that occur during bore arrival which are larger for the permeable case near the initial shoreline.
4. the drop of bed shear stress to small values values after the bore arrival and until the bed saturates at landward locations.

The backwash phase allows a detailed inspection of the BL as it grows with less influence of surface induced forces. Hence, its initial growth is essentially quasi-linear before it becomes depth limited. During backwash, the following aspects in relation to the porous media are highlighted:

1. the phase duration is progressively reduced until it is nonexistent at the landward end of the swash excursion [as suggested by *Steenhauer et al*., 2012a].
2. the TKE diffusive transport term in the surface flow shifts in sign due to exfiltration.
3. the TKE production and TKE dissipation are reduced after exfiltration takes place.
4. the time span of quasi-linear BL growth is slightly enhanced at the seaward locations where the subsurface is expected to be saturated by the time of flow reversal. FPBL theory predicts a BL rate of growth that is consistent within a factor of 2.
5. the BL growth deviates rapidly from a quasi-linear trend at the landward swash zone locations where infiltration still occurs. Under these constraints, the BL rate of growth is not well-predicted by FPBL theory.

A final outcome of the present study is given by the uprush to backwash ratios of absolute bed shear stress across the swash zone. For peak quantities, the aforementioned ratios are similar between the impermeable and permeable cases and in agreement with the direct measurements of *Barnes et al*. [2009]. The direct effect of infiltration/exfiltration is then reflected in the mean bed shear stress quantities, where the ratio is 60% higher for the permeable case in proportion to the impermeable case. Nevertheless for the tested conditions, the analysis suggests that the infiltration and exfiltration dominates over boundary layer development.

Acknowledgments

J.C. Pintado-Patiño acknowledges the financial support provided by the Mexican National Council of Science and Technology (CoNACyT) under the graduate scholarship 490080, and the Fulbright-Garcia Robles grant for his research stay at the University of Delaware. Additional funding was provided by the Instituto de Ingeniería UNAM, throughout the International Collaborative Research project with the University of Delaware, and the DGAPA UNAM (PAPIIT IN107315). J.A. Puleo was funded by the National Science Foundation (OCE-0845004 and OCE-1332703) and the University of Delaware. D. Pokrajac was funded by the UK Engineering and Physical Sciences Research Council grant 'Flood MEMORY: Multi-Event Modelling Of Risk & recoverY' (EP EP/K013513/1). The authors gratefully acknowledge Sara Corvaro, Maurizio Brocchini, Alessandro Mancinelli, Carlo Lorenzoni, Matteo Postacchini, Massimo Miozzi, for providing the data of the experiments carried out at the wave flume of the Hydraulics Laboratory of the Universit Politecnica delle Marche used for the model benchmarking. The authors also wish to thank an anonymous reviewer who provided valuable insight to improve the manuscript. The experimental data employed in this work and the numerical results can be obtained via author's request to D. Pokrajac (d.pokrajac@abdn.ac.uk) and A. Torres-Freyermuth (atorresf@iingen.unam.mx), respectively.

References

Aagaard, T., and M. G. Hughes (2006), Sediment suspension and turbulence in the swash zone of dissipative beaches, *Mar. Geol.*, *228*(1-4), 117–135, doi:10.1016/j.margeo.2006.01.003.

Antuono, M., L. Soldini, and M. Brocchini (2011), On the role of the Chezy frictional term near the shoreline, *Theor. Comput. Fluid Dyn.*, *26*(1-4), 105–116, doi:10.1007/s00162-010-0220-8.

Archetti, R., and M. Brocchini (2002), An integral swash zone model with friction: An experimental and numerical investigation, *Coastal Eng.*, *45*(2), 89–110, doi:10.1016/S0378-3839(02)00038-8.

Austin, M. J., G. Masselink, P. E. Russell, I. L. Turner, and C. E. Blenkinsopp (2011), Alongshore fluid motions in the swash zone of a sandy and gravel beach, *Coastal Eng.*, *58*(8), 690–705, doi:10.1016/j.coastaleng.2011.03.004.

Bakhtyar, R., D. Barry, A. Yeganeh-Bakhtiary, and A. Ghaheri (2009), Numerical simulation of surfswash zone motions and turbulent flow, *Adv. Water Resour.*, *32*(2), 250–263, doi:10.1016/j.advwatres.2008.11.004.

Baldock, T., and P. Nielsen (2010), Discussion of effect of seepage-induced nonhydrostatic pressure distribution on bed-load transport and bed morphodynamics by Simona Francalanci, Gary Parker, and Luca Solari, *J. Hydraul. Eng.*, *136*(1), 77–79, doi:10.1061/(ASCE)HY.1943-7900.0000015.

Baldock, T. E., and M. G. Hughes (2006), Field observations of instantaneous water slopes and horizontal pressure gradients in the swash-zone, *Cont. Shelf Res.*, *26*(5), 574–588, doi:10.1016/j.csr.2006.02.003.

Baldock, T. E., A. J. Baird, D. P. Horn, and T. Mason (2001), Measurements and modeling of swash-induced pressure gradients in the surface layers of a sand beach, *J. Geophys. Res.*, *106*(C2), 2653–2666, doi:10.1029/1999JC000170.

Barnes, M. P., and T. E. Baldock (2010), A Lagrangian model for boundary layer growth and bed shear stress in the swash zone, *Coastal Eng.*, *57*(4), 385–396, doi:10.1016/j.coastaleng.2009.11.009.

Barnes, M. P., T. O'Donoghue, J. M. Alsina, and T. E. Baldock (2009), Direct bed shear stress measurements in bore-driven swash, *Coastal Eng.*, *56*(8), 853–867, doi:10.1016/j.coastaleng.2009.04.004.
Blenkinsopp, C. E., I. L. Turner, G. Masselink, and P. E. Russell (2011), Swash zone sediment fluxes: Field observations, *Coastal Eng.*, *58*(1), 28–44, doi:10.1016/j.coastaleng.2010.08.002.
Briganti, R., N. Dodd, D. Pokrajac, and T. O'Donoghue (2011), Non linear shallow water modelling of bore-driven swash: Description of the bottom boundary layer, *Coastal Eng.*, *58*(6), 463–477, doi:10.1016/j.coastaleng.2011.01.004.
Brocchini, M., and T. E. Baldock (2008), Recent advances in modeling swash zone dynamics: Influence of surf-swash interaction on nearshore hydrodynamics and morphodynamics, *Rev. Geophys.*, *46*, RG3003, doi:10.1029/2006RG000215.
Butt, T., and P. Russell (1999), Suspended sediment transport mechanisms in high-energy swash, *Mar. Geol.*, *161*, 361–375.
Butt, T., P. Russell, and I. Turner (2001), The influence of swash infiltrationexfiltration on beach face sediment transport: Onshore or offshore?, *Coastal Eng.*, *42*(1), 35–52, doi:10.1016/S0378-3839(00)00046-6.
Butt, T., P. Russell, J. Puleo, J. Miles, and G. Masselink (2004), The influence of bore turbulence on sediment transport in the swash and inner surf zones, *Cont. Shelf Res.*, *24*(78), 757–771, doi:10.1016/j.csr.2004.02.002.
Chorin, A. J. (1969), On the convergence of discrete approximations to the Navier-Stokes equations, *Math. Comput.*, *23*(106), 341–353, doi:10.1090/S0025-5718-1969-0242393-5.
Conley, D. C., and D. L. Inman (1994), Ventilated oscillatory boundary layers, *J. Fluid Mech.*, *273*, 261–284, doi:10.1017/S002211209400193X.
Corvaro, S., A. Mancinelli, M. Brocchini, E. Seta, and C. Lorenzoni (2010), On the wave damping due to a permeable seabed, *Coastal Eng.*, *57*(1112), 1029–1041, doi:10.1016/j.coastaleng.2010.06.005.
Corvaro, S., M. Miozzi, M. Postacchini, A. Mancinelli, and M. Brocchini (2014), Fluid-particle interaction and generation of coherent structures over permeable beds: An experimental analysis, *Adv. Water Resour.*, *72*, 97–109, doi:10.1016/j.advwatres.2014.05.015.
Cowen, E. A., I. M. Sou, P. L.-F. Liu, and B. Raubenheimer (2003), Particle image velocimetry measurements within laboratory-generated swash zone, *J. Eng. Mech.*, *129*, 1119–1129.
Cox, D. T., W. A. Hobensack, and A. Sukumaran (2001), Bottom stress in the inner surf and swash zone, in *Coastal Engineering 2000*, edited by B. L. Edge, *Proceedings 27th International Conference on Coastal Engineering 2000*, ASCE, pp. 108–119, doi:10.1061/40549(276)9.
Desombre, J., D. Morichon, and M. Mory (2013), RANS v2f simulation of a swash event: Detailed flow structure, *Coastal Eng.*, *71*, 1–12, doi:10.1016/j.coastaleng.2012.07.001.
Fredsøe, J., and R. Deigaard (1992), *Mechanics of Coastal Sediment Transport, Adv. Ser. Ocean Eng.*, vol. 3, World Sci., Singapore.
Hirt, C. W., and B. D. Nichols (1981), Volume of fluid (VOF) method for the dynamics of free boundaries, *J. Comput. Phys.*, *39*(1), 201–225, doi:10.1016/0021-9991(81)90145-5.
Horn, D. P. (2006), Measurements and modelling of beach groundwater flow in the swash-zone: A review, *Cont. Shelf Res.*, *26*(5), 622–652, doi:10.1016/j.csr.2006.02.001.
Hsu, T.-J., T. Sakakiyama, and P. L. F. Liu (2002), A numerical model for wave motions and turbulence flows in front of a composite breakwater, *Coastal Eng.*, *46*(1), 25–50, doi:10.1016/S0378-3839(02)00045-5.
Hughes, M., and I. Turner (1999), The beachface, in edited by A. D. Short, *Handbook of Beach and Shoreface Morphodynamics*, pp. 119–144, Wiley, Chichester, U. K.
Hughes, M. G., T. Aagaard, and T. E. Baldock (2007), Suspended sediment in the swash zone: Heuristic analysis of spatial and temporal variations in concentration, *J. Coastal Res.*, *23*(6), 1345–1354, doi:10.2112/05-0531.1.
Jackson, N. L., G. Masselink, and K. F. Nordstrom (2004), The role of bore collapse and local shear stresses on the spatial distribution of sediment load in the uprush of an intermediate-state beach, *Mar. Geol.*, *203*(12), 109–118, doi:10.1016/S0025-3227(03)00328-1.
Karambas, T. V. (2003), Modelling of infiltration-exfiltration effects of cross-shore sediment transport in the swash zone, *Coastal Eng. J.*, *45*(01), 63–82, doi:10.1142/S057856340300066X.
Kikkert, G. A., T. O'Donoghue, D. Pokrajac, and N. Dodd (2012), Experimental study of bore-driven swash hydrodynamics on impermeable rough slopes, *Coastal Eng.*, *60*, 149–166, doi:10.1016/j.coastaleng.2011.09.006.
Kikkert, G. A., D. Pokrajac, T. O'Donoghue, and K. Steenhauer (2013), Experimental study of bore-driven swash hydrodynamics on permeable rough slopes, *Coastal Eng.*, *79*, 42–56, doi:10.1016/j.coastaleng.2013.04.008.
Lanckriet, T., and J. A. Puleo (2013), Near-bed turbulence dissipation measurements in the inner surf and swash zone, *J. Geophys. Res. Oceans*, *118*, 6634–6647, doi:10.1002/2013JC009251.
Lanckriet, T., J. Puleo, G. Masselink, I. Turner, D. Conley, C. Blenkinsopp, and P. Russell (2014), Comprehensive Field Study of Swash-Zone Processes. II: Sheet Flow Sediment Concentrations during Quasi-Steady Backwash, *J. Waterw. Port Coastal Ocean Eng.*, *140*(1), 29–42, doi:10.1061/(ASCE)WW.1943-5460.0000209.
Lara, J. L., N. Garcia, and I. J. Losada (2006a), RANS modelling applied to random wave interaction with submerged permeable structures, *Coastal Eng.*, *53*(56), 395–417, doi:10.1016/j.coastaleng.2005.11.003.
Lara, J. L., I. J. Losada, and P. L.-F. Liu (2006b), Breaking waves over a mild gravel slope: Experimental and numerical analysis, *J. Geophys. Res.*, *111*, C11019, doi:10.1029/2005JC003374.
Lara, J. L., I. J. Losada, and R. Guanche (2008), Wave interaction with low-mound breakwaters using a RANS model, *Ocean Eng.*, *35*(13), 1388–1400, doi:10.1016/j.oceaneng.2008.05.006.
Li, L., D. A. Barry, and C. B. Pattiaratchi (1997), Numerical modelling of tide-induced beach water table fluctuations, *Coastal Eng.*, *30*(12), 105–123, doi:10.1016/S0378-3839(96)00038-5.
Li, L., D. A. Barry, F. Stagnitti, and J.-Y. Parlange (2000), Groundwater waves in a coastal aquifer: A new governing equation including vertical effects and capillarity, *Water Resour. Res.*, *36*(2), 411–420, doi:10.1029/1999WR900307.
Lin, P., and P. L.-F. Liu (1998a), A numerical study of breaking waves in the surf zone, *J. Fluid Mech.*, *359*, 239–264, doi:10.1017/S002211209700846X.
Lin, P., and P. L.-F. Liu (1998b), Turbulence transport, vorticity dynamics, and solute mixing under plunging breaking waves in surf zone, *J. Geophys. Res.*, *103*(C8), 15,677–15,694, doi:10.1029/98JC01360.
Liu, P. L.-F., P. Lin, K.-A. Chang, and T. Sakakiyama (1999), Numerical modeling of wave interaction with porous structures, *J. Waterw. Port Coastal Ocean Eng.*, *125*(6), 322–330, doi:10.1061/(ASCE)0733-950X(1999)125:6(322).
Liu, Y., P. MacCready, B. M. Hickey, E. P. Dever, P. M. Kosro, and N. S. Banas (2009), Evaluation of a coastal ocean circulation model for the Columbia River plume in summer 2004, *J. Geophys. Res.*, *114*, C00B04, doi:10.1029/2008JC004929.
Lohmann, I. P., J. Fredse, B. M. Sumer, and E. D. Christensen (2006), Large Eddy Simulation of the ventilated wave boundary layer, *J. Geophys. Res.*, *111*, C06036, doi:10.1029/2005JC002946.
Longo, S., M. Petti, and I. J. Losada (2002), Turbulence in the swash and surf zones: A review, *Coastal Eng.*, *45*(34), 129–147, doi:10.1016/S0378-3839(02)00031-5.

Losada, I. J., J. L. Lara, R. Guanche, and J. M. Gonzalez-Ondina (2008), Numerical analysis of wave overtopping of rubble mound breakwaters, *Coastal Eng.*, *55*(1), 47–62, doi:10.1016/j.coastaleng.2007.06.003.
Masselink, G., and J. A. Puleo (2006), Swash-zone morphodynamics, *Cont.Shelf Res.*, *26*(5), 661–680, doi:10.1016/j.csr.2006.01.015.
Masselink, G., D. Evans, M. G. Hughes, and P. Russell (2005), Suspended sediment transport in the swash zone of a dissipative beach, *Mar. Geol.*, *216*(3), 169–189, doi:10.1016/j.margeo.2005.02.017.
Masselink, G., P. Russell, I. Turner, and C. Blenkinsopp (2009), Net sediment transport and morphological change in the swash zone of a high-energy sandy beach from swash event to tidal cycle time scales, *Mar. Geol.*, *267*(12), 18–35, doi:10.1016/j.margeo.2009.09.003.
Mory, M., S. Abadie, S. Mauriet, and P. Lubin (2011), Run-up flow of a collapsing bore over a beach, *Eur. J. Mech.*, *30*(6), 565–576, doi:10.1016/j.euromechflu.2010.11.005.
Nakayama, A., and F. Kuwahara (1999), A macroscopic turbulence model for flow in a porous medium, *J. Fluids Eng.*, *121*(2), 427–433, doi:10.1115/1.2822227.
Nielsen, P. (1992), Coastal Bottom Boundary Layers and Sediment Transport, *Adv. Ser. Ocean Eng.*, vol. 4, World Sci., Singapore.
Nielsen, P., S. Robert, B. Mller-Christiansen, and P. Oliva (2001), Infiltration effects on sediment mobility under waves, *Coastal Eng.*, *42*(2), 105–114, doi:10.1016/S0378-3839(00)00051-X.
O'Donoghue, T., D. Pokrajac, and L. Hondebrink (2010), Laboratory and numerical study of dambreak-generated swash on impermeable slopes, *Coastal Eng.*, *57*(5), 513–530, doi:10.1016/j.coastaleng.2009.12.007.
Osborne, P. D., and G. A. Rooker (1999), Sand re-suspension events in a high energy infragravity swash zone, *J. Coastal Res.*, *15*(1), 74–86.
Packwood, A. R., and D. H. Peregrine (1979), The propagation of solitary waves and bores over a porous bed, *Coastal Eng.*, *3*, 221–242, doi:10.1016/0378-3839(79)90022-X.
Petti, M., and S. Longo (2001), Turbulence experiments in the swash zone, *Coastal Eng.*, *43*(1), 1–24, doi:10.1016/S0378-3839(00)00068-5.
Pope, S. B. (2000), *Turbulent Flows*, 1 ed., Cambridge Univ. Press, Cambridge, U. K.
Puleo, J. A., and K. T. Holland (2001), Estimating swash zone friction coefficients on a sandy beach, *Coastal Eng.*, *43*(1), 25–40, doi:10.1016/S0378-3839(01)00004-7.
Puleo, J. A., R. A. Beach, R. A. Holman, and J. S. Allen (2000), Swash zone sediment suspension and transport and the importance of bore-generated turbulence, *J. Geophys. Res.*, *105*(C7), 17,021–17,044, doi:10.1029/2000JC900024.
Puleo, J. A., T. Lanckriet, and P. Wang (2012), Near bed cross-shore velocity profiles, bed shear stress and friction on the foreshore of a microtidal beach, *Coastal Eng.*, *68*, 6–16, doi:10.1016/j.coastaleng.2012.04.007.
Puleo, J. A., et al. (2014a), Comprehensive field study of swash-zone processes. I: Experimental design with examples of hydrodynamic and sediment transport measurements, *J. Waterw. Port Coastal Ocean Eng.*, *140*(1), 14–28, doi:10.1061/(ASCE)WW.1943-5460.0000210.
Puleo, J. A., T. Lanckriet, and C. Blenkinsopp (2014b), Bed level fluctuations in the inner surf and swash zone of a dissipative beach, *Mar. Geol.*, *349*, 99–112, doi:10.1016/j.margeo.2014.01.006.
Raubenheimer, B., S. Elgar, and R. T. Guza (2004), Observations of swash zone velocities: A note on friction coefficients, *J. Geophys. Res.*, *109*, C01027, doi:10.1029/2003JC001877.
Schlichting, H., and K. Gersten (2000), *Boundary-Layer Theory*, 8th ed., Springer, Berlin.
Shih, T.-H., J. Zhu, and J. L. Lumley (1996), Calculation of wall-bounded complex flows and free shear flows, *Int. J. Numer. Methods Fluids*, *23*(11), 1133–1144, doi:10.1002/(SICI)1097-0363(19961215)23:11¡1133::AID-FLD456¿3.0.CO;2-A.
Sleath, J. F. A. (1984), *Sea Bed Mechanics*, John Wiley, N. Y.
Sou, I. M., and H. Yeh (2011), Laboratory study of the cross-shore flow structure in the surf and swash zones, *J. Geophys. Res.*, *116*, C03002, doi:10.1029/2010JC006700.
Sou, I. M., E. A. Cowen, and P. L.-F. Liu (2010), Evolution of the turbulence structure in the surf and swash zones, *J. Fluid Mech.*, *644*, 193–216, doi:10.1017/S0022112009992321.
Sparrow, K., D. Pokrajac, and A. D. Van der A (2012), The effect of bed permeability on oscillatory boundary layer flow, *Coastal Eng. Proc.*, *1*(33), waves.26, doi:10.9753/icce.v33.waves.26.
Steenhauer, K., D. Pokrajac, T. O'Donoghue, and G. A. Kikkert (2011), Subsurface processes generated by bore-driven swash on coarse-grained beaches, *J. Geophys. Res.*, *116*, C04013, doi:10.1029/2010JC006789.
Steenhauer, K., D. Pokrajac, and T. O'Donoghue (2012a), Numerical model of swash motion and air entrapment within coarse-grained beaches, *Coastal Eng.*, *64*, 113–126, doi:10.1016/j.coastaleng.2012.01.004.
Steenhauer, K., D. Pokrajac, and T. O'Donoghue (2012b), Implementation of ADER scheme for a bore on an unsaturated permeable slope, *Int. J. Numer. Methods Fluids*, *70*(6), 682–702, doi:10.1002/fld.2706.
Torres-Freyermuth, A., J. A. Puleo, and D. Pokrajac (2013), Modeling swash-zone hydrodynamics and shear stresses on planar slopes using Reynolds-Averaged NavierStokes equations, *J. Geophys. Res. Oceans*, *118*, 1019–1033, doi:10.1002/jgrc.20074.
Turner, I. L., and G. Masselink (1998), Swash infiltration-exfiltration and sediment transport, *J. Geophys. Res.*, *103*(C13), 30,813–30,824, doi:10.1029/98JC02606.
Turner, I. L., and P. Nielsen (1997), Rapid water table fluctuations within the beach face: Implications for swash zone sediment mobility?, *Coastal Eng.*, *32*(1), 45–59, doi:10.1016/S0378-3839(97)00015-X.
van Gent, M. R. A. (1994), The modelling of wave action on and in coastal structures, *Coastal Eng.*, *22*(34), 311–339, doi:10.1016/0378-3839(94)90041-8.
Wang, P., B. A. Ebersole, E. R. Smith, and B. D. Johnson (2002), Temporal and spatial variations of surf-zone currents and suspended sediment concentration, *Coastal Eng.*, *46*(3), 175–211, doi:10.1016/S0378-3839(02)00091-1.
Willmott, C. J., S. G. Ackleson, R. E. Davis, J. J. Feddema, K. M. Klink, D. R. Legates, J. O'Donnell, and C. M. Rowe (1985), Statistics for the evaluation and comparison of models, *J. Geophys. Res.*, *90*(C5), 8995–9005, doi:10.1029/JC090iC05p08995.
Zhang, Q., and P. L. F. Liu (2008), A numerical study of swash flows generated by bores, *Coastal Eng.*, *55*(12), 1113–1134, doi:10.1016/j.coastaleng.2008.04.010.
Zhu, F., and N. Dodd (2013), Net beach change in the swash zone: A numerical investigation, *Adv. Water Resour.*, *53*, 12–22, doi:10.1016/j.advwatres.2012.10.002.